ISSN: 2349 - 4891
International
Journal of Recent Research and Applied Studies
(Multidisciplinary Open Access Refereed e-Journal)

Stress base modelling and computer simulation of drop-weight impact response of composite panels with domain partitioning and adaptive meshing techniques

Umar Farooq[1] and Peter Myler[2]

[1]Reader, Department of Engineering, Support and Advance Sciences, University of Bolton, Bolton BL3 5AB UK

[2]Professor, Head of Engineering, Support and Advance Sciences, University of Bolton, Bolton BL3 5AB UK

Received 15st March 2021, Accepted 7st April 202

Abstract

This work is concerned with stress base computer modelling and simulation to predict low-velocity drop-weight impact response of carbon fibre reinforced composite panels. The composites are being extensively used as building-block of aircraft structures. During service life of an aircraft fuselage and wings may suffer accidental tool (box) drop impact due to their vulnerable locations. The impact could cause severe invisible damage that grows during future operations and may result in catastrophic failure. Most of the previous studies to avert the damage are experimental, based on load-deflection methodology, neglect effects of through-thickness stresses, and lack in predicting all possible failures as well as require huge efforts, time, and resources. Computer simulations are needed for more reliable pre-design stage analyses. Current study describes limitations of experimental testing in ply-level predictions, mathematical formulation of stresses, and computer simulations in ABAQUS™/ Explicit software. Domain under impactor nose-tips was partitioned to obtain dense discretisation using adaptive meshing scheme to efficiently predict two-dimensional stresses. Three-dimensional stresses were computed from two-dimensional predicted stresses via numerical integration program in MATALAB™. The predicted stresses were then utilised in mode-based failure criteria to predict ply-level failures in MATALAB™ program. Data analyses were performed with MS Excel™ tabular and graphic plot forms. Results were compared with published data results and found within agreement up to 90%. Based on acceptable predictions, the study is proposed to investigate similar other problems to predict more possible ply-level failures.

Key words: *Fibrous Composites; Low-velocity Impact; Domain Partitioning; Adaptive Meshing; Explicit Dynamic Methods.*

Abstract

This work is concerned with stress base computer modelling and simulation to predict low-velocity drop-weight impact response of carbon fibre reinforced composite panels. The composites are being extensively used as building-block of aircraft structures. During service life of an aircraft fuselage and wings may suffer accidental tool (box) drop impact due to their vulnerable locations. The impact could cause severe invisible damage that grows during future operations and may result in catastrophic failure. Most of the previous studies to avert the damage are experimental, based on load-deflection methodology, neglect effects of through-thickness stresses, and lack in predicting all possible failures as well as require huge efforts, time, and resources. Computer simulations are needed for more reliable pre-design stage analyses. Current study describes limitations of experimental testing in ply-level predictions, mathematical formulation of stresses, and computer simulations in ABAQUS™/ Explicit software. Domain under impactor nose-tips was partitioned to obtain dense discretisation using adaptive meshing scheme to efficiently predict two-dimensional stresses. Three-dimensional stresses were computed from two-dimensional predicted stresses via numerical integration program in MATALAB™. The predicted stresses were then utilised in mode-based failure criteria to predict ply-level failures in MATALAB™ program. Data analyses were performed with MS Excel™ tabular and graphic plot forms. Results were compared with published data results and found within agreement up to 90%. Based on acceptable predictions, the study is proposed to investigate similar other problems to predict more possible ply-level failures.

Keywords: Fibrous Composites; Low-velocity Impact; Domain Partitioning; Adaptive Meshing; Explicit Dynamic Methods.

1. Introduction

Carbon fibre reinforced composites are being widely used in aerospace industry due to their high strength and stiffness ratios to weight, excellent mechanical properties, and tailoring potential to structural components [1]. However, wings and fuselage of aircrafts are prone to accidental drop-weight

Correspondence

Umar Farooq
Reader, Department of Engineering, Support and Advance Sciences, University of Bolton, Bolton BL3 5AB UK

impact by tool box, hammer, and spanner during part assembly, maintenance, and service life [2]. Such flat-nose impacts may cause damage that cannot be detected through routine inspections. Since aircraft parts are brittle in nature, absorb less impact energy, have no through-thickness reinforcements [3], hence exhibit low deformation resistance prior to cracking, delamination and fracture. As on-board damage detection, repair, or healing facilities are not available for malfunctioning parts. Thus impact-induced damage could grow and spread due to continuous operations that could result in unexpected catastrophic failure. The catastrophic failures result in loss of human lives and structural assets. That is a major concern to the aircraft industry. Thus, a greater need exists to understand the impact response of composites made parts at pre-design stage to mitigate impact-induced damage and avert pre-mature failure as well as for safe, reliable, economical, and comfortable use of aircrafts. Extensive efforts by a significant body of researchers are underway to improve integrity of structural components so that aircrafts could safely reach and land at nearest airport to avert catastrophic failure once damage is detected. Literature on impact of composite panels consists of vast and diverse fields such as impact event, damage detection, resistance, and tolerance, so more relevant and selected studies are being presented.

Experimental studies based on the American Standard Test Method (ASTM D7136) for measuring damage resistance of composites to a drop-weight impact using Dynatup 9250HV test machine are referred in [4]. The drop-weight tests made possible to identify parameters that allow characterization of load threshold for first failure in composite panels to correlate drop in load-time history curve. Similarly, variation in energy-time curve such as peak energy is equivalent to the impact energy (the energy needed to stop the impactor), the energy absorbed by the target panel, and total energy transferred (dissipated energy which is equal to the impact energy in the rebound case) [5]. Comparison of curves interpreted maximum impact force, velocity-time history, load-deflection, and energy-time/deflection in parametric studies [6]. However, the drop-weight test methods are time consuming, expensive, and test results have large dispersibility [7]. While quasi-static indentation simulation test as an alternative to impact event was proposed in [8] where damage initiation and propagation were detected relatively easily, deflection was directly measured with greater accuracy, and maximal transverse load remained under control. The quasi-static indentation models provided in-depth study of the damage mechanisms and progression at different impact event stages [9], [10].

The study correlating damage-mode to impactor's shape found that damage initiation threshold load increases under blunter-tip impactors [11]. Another similar study [12] proposed that blunter-tip impactors create greater contact area, less concentrated pressure, and caused lesser dent than sharper-tip impactors. Effects of blunter-tip impactors' were also reported to be more significant on impact of relatively thin panels and created more de-lamination [13]. The sharper-tip impactors create more fibre damage [14]. Furthermore, blunter tip impactors create less fibre damage, reduction in tensile as well as compressive strength [15]. Analytical treatment demonstrated in [16] influence of impact parameters on panels adjusted to come up with real object impacts of ogival, truncated, flat, hemi-spherical, and conical ended shapes.

Studied involving stress based failure criteria on unidirectional fibre composites are reported in [17], [18]. Initial damages in the form of cracking or de-lamination were observed to be difficult to detect [19]. As the damages do not significantly reduce stiffness instead serve as flaws that allow de-lamination up to fibre breakage [20], [22]. The study in [1] reported that de-lamination is a result of transverse shear stresses found roughly halfway through the thickness of the laminated panels [24]. Higher stresses from impacted zone under impactor's nose-tips were used to predict ply-by-ply failure in a mode-base failure criterion [25]. Interaction between de-lamination cracks and transverse matrix cracks where interactions between these two damage modes were recorded can be found in [26], [27]. The study [28] compiled detailed interactions between de-laminations and matrix cracks for various layups of composites. Failure initiation in composite structures was predicted due to excessive stresses under low-velocity impact in [29]. Intra-laminar failure mechanisms of composites found that the same incident energy with different combinations of impactor mass and velocity can have different effects on the impact response [30], [31].

References on finite element modelling of impact-induced damage in composites can be found in [32]. Simulations modelling demonstrated ability to correlate the onset and extent of damage [33]. Capability of commercial software is rapidly growing and evolving to integrate inter-disciplinary simulation packages [34]. Large amount of data were correlated via curve fit basis to simple algebraic formulations in performance characteristics of materials and components for particular design objectives [35]. Simulations developed in commercial software packages are making available the fast predictive tools for pre-design analysis with ease of creating simulation model, data and result interpretations, and graphic and visual insight into the ply-level damage mechanisms [36], [37]. Rapidly evolving simulations into viable design tools promote extensive finite element analyses, as industries have also integrated simulation into part of their design process to economically achieve higher efficiency [38]. Simulations performed to supplement experimental testing for prediction of impact-induced damage can be found in [39], [40]. Delamination or matrix crack alone was introduced assigning two different node numbers to each node (to prevent interpenetration of surfaces) connected through interface elements available in ABAQUS™ in [1] where four node numbers were introduced when delamination and matrix crack intersect. Delamination of the required length was introduced between plies by intersecting interface between the elements. Matrix cracking was modelled in a similar manner by introducing interface elements between the first and second of elements closet to the y-axis. Simulations were carried out to compute inter-laminar stresses from two-dimensional modelling [42]. However, impact damage prediction in carbon composite structures revealed convergence and mesh dependency challenges faced in the numerical studies [43]. Moreover, the extrapolated information provides little understanding about underlying damage mechanisms and cannot be generally reliable [44].

The literature review reveals that majority of the previous studies are experimental, simulations are based on two-dimensional stresses where through-thickness stresses are neglected, and fine mesh for damage zone under impactor-tip were not considered; therefore, could not predict all possible failed plies. An efficient simulation model is needed to predict more reliable low velocity impact-induced damage and failure of fibrous composites.

Current study is based on experimental testing, mathematical evolution of stress based formulation, and efficient computer simulations. Experimental study demonstrates limitations with data logging as well as ply-level analysis. Two simulation models were developed in commercially available software package ABAQUS™/Explicit according to procedures in [33], [34]. Simulation models consisting of un-partitioned and partitioned domain under impactor nose tips were developed to generate dense meshes with fine elements using adaptive meshing scheme. Two-dimensional stresses were predicted to utilise in equilibrium equations discretized with forward differencing schemes and numerically integrated using quadratic polynomial based modified Simpson rule programmed in MATLAB™ software to predict three-dimensional stresses. The predicted three-dimensional stresses were then utilized in the formulation set of advanced failure criteria in another MATLAB™ program to predict ply-by-ply fibre-fracture, matrix-cracks, and quadratic de-lamination failure modes. Selected results were compared and validated against data results available in the literature and found to be within acceptable (±10) deviations. Some of the selected results have been presented.

2. Materials and methods

2.1 Composite panels and impactors with material properties, and impact tester

The panels considered herein are made of aerospace grade carbon fibre-reinforced infused with toughened epoxy-resin matrix of properties code Fibre dux 914C-833-40 with embedded fibre horns technique of every fifth layer. Symmetrical layups consisted of construction code $[0/45/-45/90]_{ns}$ where subscript 's' stands for symmetric and 'n' varies from 1, 2, and 3 for sequence repetitions. The panels manufactured by Aircellece™ consist of 8-, 16-, and 24-Ply layups with variable thicknesses of 2.4(±0.06), 4.8(±0.08), and 7.2(±0.12)mm respectively. Schematics of panels consisted of 150mm x 120mm areas of European Standard (equivalent to Boeing™ USA Standard), satin weave layups, and impact affected area shown below in **FIGURE 1**. Material properties of the industry provided panels are given in **TABLE 1**.

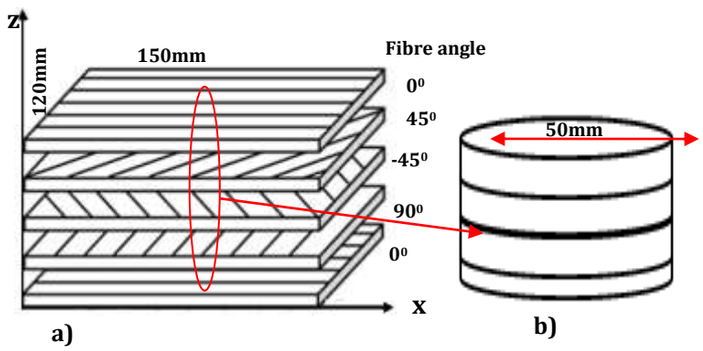

FIGURE 1: Schematics of a) Satin weave 5th harness symmetric panels, b) impact affected area

TABLE 1: Material properties of composite panels [20]

Property	Fibredux 914C-833-40	Units
Tensile Modulus (E_{11})	230	GPa
Tensile Modulus ($E_{22} = E_{33}$)	21	GPa
In-plane Shear Modulus ($G_{12} = G_{13}$)	88	GPa
Out-of-plane Shear Modulus (G_{23})	11	GPa
Poisson's Ratio (ν_{12})	0.2	-
Longitudinal Tensile Strength (X_T)	1453	MPa
In-plane Shear Strength (S_{12})	180	MPa
Longitudinal Compressive Strength (Y_T)	650	MPa
Transverse shear strength ($S_{13} = S_{23}$)	32	MPa
Inter-laminar shear strength (Z_T)	10	MPa

Since panels are especially orthotropic and transversally isotropic; the constants are $G_{13} = G_{12}$; $E_2 = E_3$; $\nu_{21} = \nu_{31}$, and $\nu_{23} = \nu_{32}$. In addition, the relationship among the isotropic engineering constants $G_{23} = \frac{E_2}{2(1+\nu_{32})}$ is valid associated with the 23 plane. The total average thickness of every plies in a specific lay-up was assumed to be of uniform material properties. Impactors were made of stainless steel having material properties of Young's modulus 210GPa and Poisson's ratio 0.3. Impactors have shank of diameter 20mm that reduces to 10±(0.18)mm. The round-nose impactor has nose-tip of 5±(0.15)mm while flat nose impactor a ground flat nose impact face. All impact tests were conducted using the state-of-the-art INSTRON™ 9250HV impact machine available at the Bolton University in accordance with round and flat nose impactors used to conduct testing shown in **FIGURE 2**. Drop-weight impacts occurred at central location on panels consisting of pre-assumed uniform ply thickness, perfect bonding among plies panels, and fully clamped around the edges. Experimental procedure, impact elapse time (1.1micro-seconds), drop-weight impactors (lump mass), and range of velocity amplitudes (1.6-4.9m/s) were selected from ASTM [4], [20].

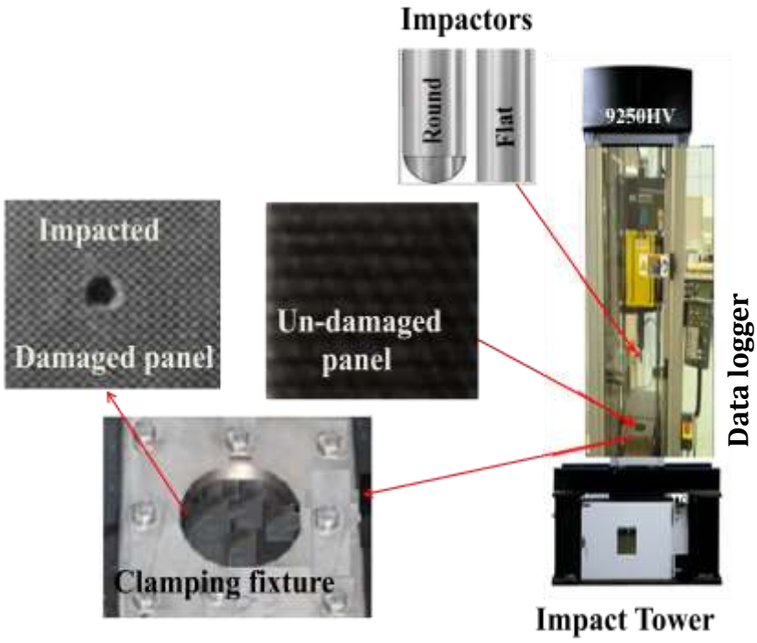

FIGURE 2: Impact tester 9250HV machine [4].

2.2 Post-impact non-destructive damage detection and approximation techniques

2.2.1 Conventional C-scanning of impacted panels

Most of the reported non-destructive techniques to collaborate in post-impact damage diagnostics and failure status are visual inspections and data analysis. Visible damage may be seen using non-destructive conventional c-scan machines in two dimensions where multi-plane damage is projected on a single plane as depicted in **FIGURE 3** below [20]. Such damages are approximated from summation of small elements by imposing grid on oval or circular shape image snapped to rectangular mesh. A coordinate system is imposed to locate initial and final positions of the diameter of the damaged area in xy-plane. Then area is calculated from circle or ellipse formula that approximate to map on image by adding or subtracting rectangular mesh elements or cells. To predict percentage ratio of delaminated area, the delaminated area is divided by the panel area. The MATLAB™ program to approximate percentage ratios of damage areas given in [34] is modified shown in **TABLE 2**.

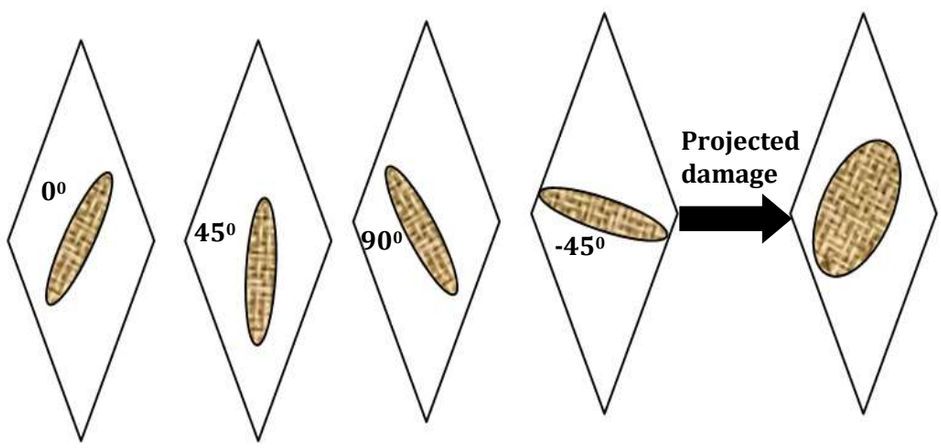

FIGURE 3: Schematic of multiply damage projection onto outer surface of single ply

TABLE 2: MATLAB™ program for prediction of damage zones [34]

```
fprintf('=============================================================================================\n');
fprintf('||          MATLAB program to predict overall surface damage percentage of impacted panels                    ||\n');
fprintf('=============================================================================================\n\n');
%Generate gridlines on surface of panel to demarcate damage zone by approximate two points in x-, y-directions
disp('PLEASE ENTER  LENGTH AND  WDTH OF PANEL')
Length=input('Please enter length of panel > 1'); disp(Length); Width= input('Please enter width of panel > 1'); disp(Width)
Panel_Area = Length*Width; fprintf('Panel-Area =%f ', Panel_Area); disp('PLEASE ENTER X-, Y-COORDINATES OF DAMAGED AREA')
x1_coordinate1=input('Enter first x-position from first point'); disp(x1_coordinate1)
x2_coordinate2=input('Enter second  x-point from second point'); disp(x2_coordinate2)
xx=( x2_coordinate2- x1_coordinate1)^2; %approximate distance in x-direction
y1_coordinate1=input('Enter first y-position from first point'); disp(y1_coordinate1)
y2_coordinate2=input('Enter second  y-position from second point'); disp(y_coordinate2)
yy=( y2_coordinate2- y1_coordinate1)^2; damaged_zone_diamater= sqrt(xx+yy);
Elliptical_damage_zone = pi*xx*yy; fprinf('Elliptical_damage_zone = %f', Damage_zone_area);
Damage_zone_area= pi*(damaged_zone_diameter/2)^2; fprinf('Damage_zone_area = %f', Damage_zone_area);
%Panel damage percentage prediction; Percentage_Damaged_Panel = (Damage_zone_area/Panel_Area)*100;
fprintf('===========Damage Percentage of Panel ======\n'); fprintf(' ----------------------\n\n')
fprintf('The approximate percentage of panel damage is =%f', Percentage_Damaged_Panel)
```

2.2.2 Post-processing and analysis of impact test generated data

Data analysis techniques are applied to quantify, visualize, and supplement the damage diagnostics and approximation. A plotted curve depicts impact response of the panel for the whole impact duration while impact is a result of the local deformation required for the surfaces of panel and impactor to conform in the contact area. Neglecting influence of panel thickness, the time histories of the permanent central deflection of the panels are approximated as the displacement of the impactor during the impact process. A typical force-history plot is shown and deformation **FIGURE 4**. At lower impact energy values, near the damage threshold, the values of critical and peak force coincide. Whereas at even lower values they lose significance, in the sense that failure does not occur. It can be seen from the plot that when the impact force reaches a threshold value, there is unstable crack propagation leading to instantaneous large delaminated areas. This often causes the impact force to drop in the response, indicating sudden loss of stiffness. The critical force (threshold load) represents the initial value at which a significant change in the stiffness properties of the panel can be detected. The typical history of the impact force for monolithic specimens where the threshold loads and the peak force are identified can be interpreted to study the panel response. And then the force deflection curves could be obtained by combining the force-time and displacement-time curves **FIGURE 4(b)**. In addition, the impact energy limit of the panels was another important aspect to characterize the impact resistance of the materials, which could be obtained based on the external damage pattern observations **FIGURE 4(c)**. Similarly, depending on the impact velocity, critical force could be equal to peak force. Graphic plots not only create visual link to associate damage and failure modes but also provide invaluable benchmarking tools for correlation to group and categorize impact damage mechanisms: initiation, propagation, and penetration as shown in **FIGURE 4(d)** [5], [20].

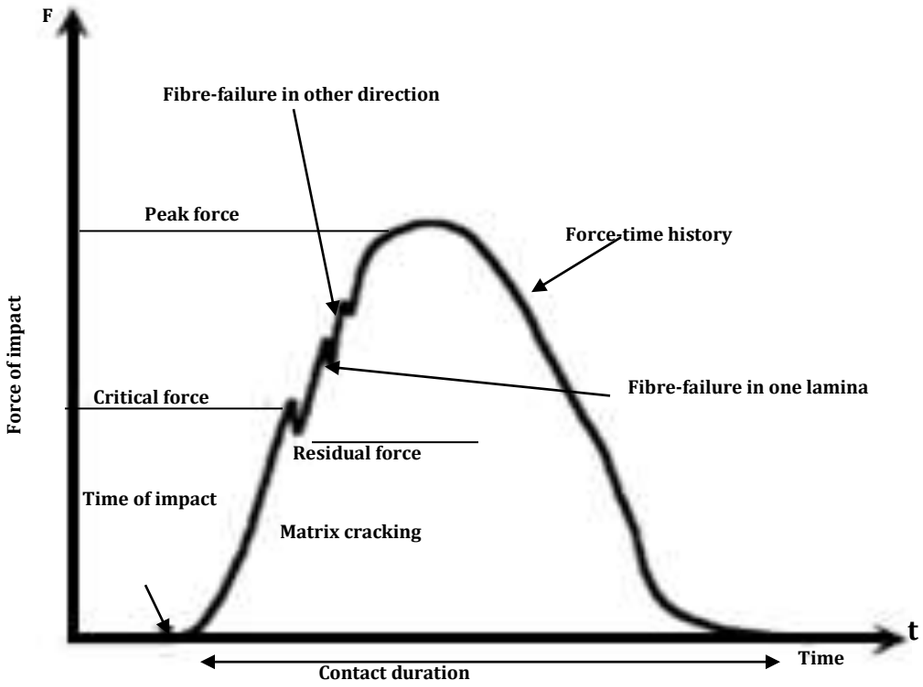

a) Force-time history modified and deformation event during loading phase

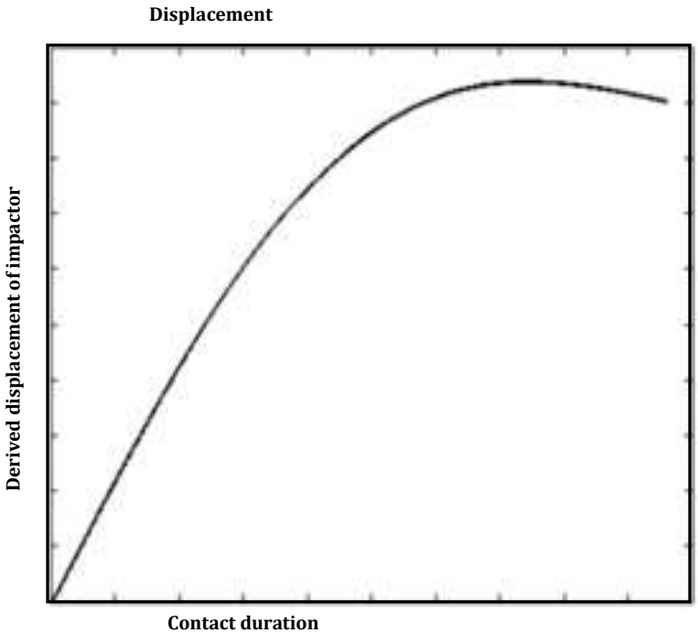

b) Displacement-time history load drops during impact phase

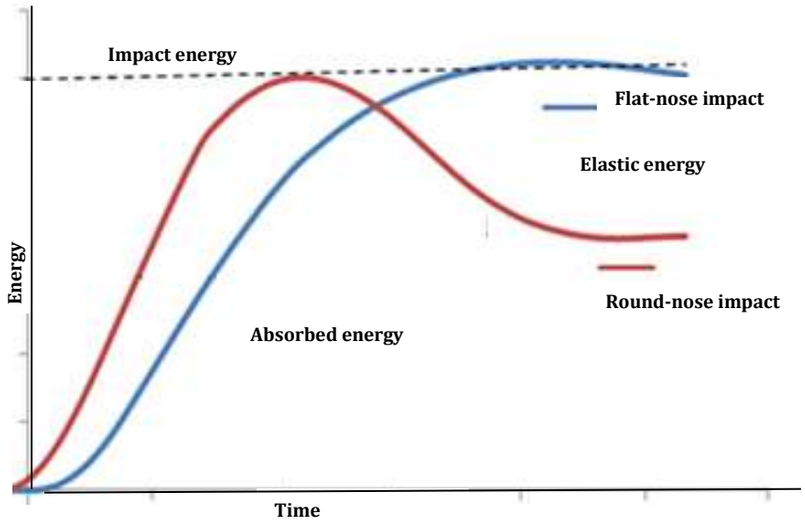

c) Energy/time curve as area under impactor nose

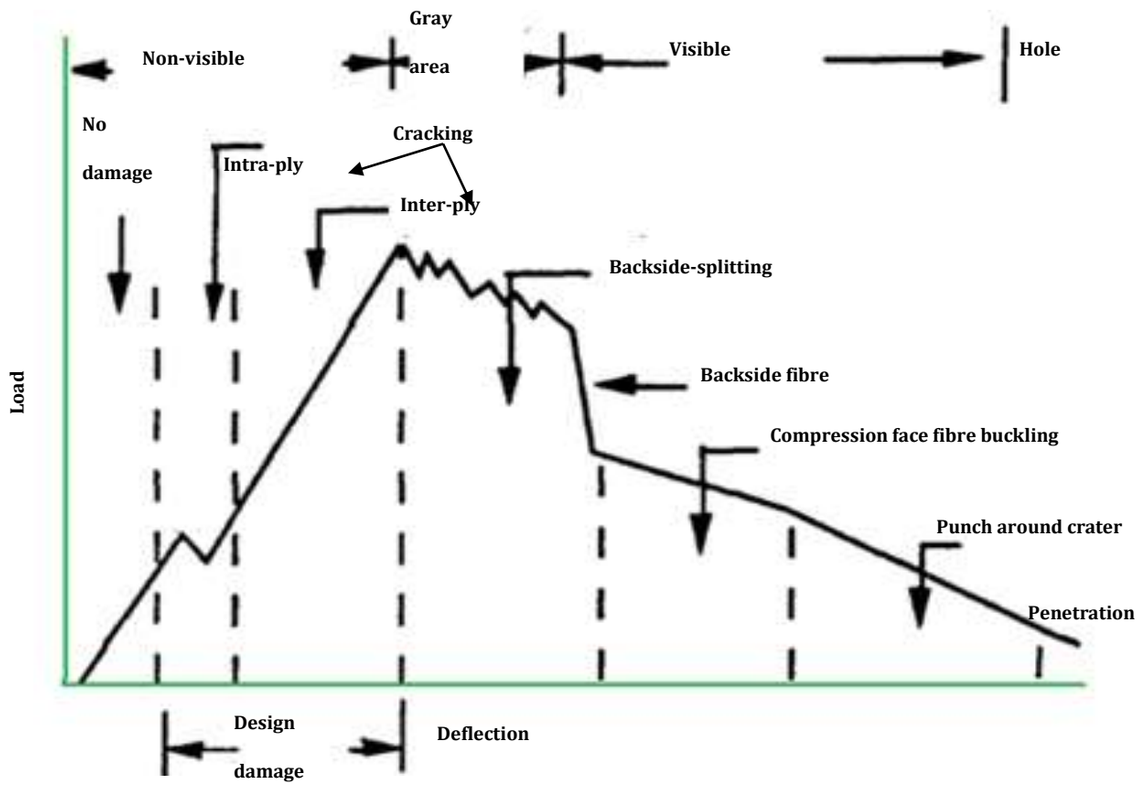

d) Correlation of load to impact-induced damage modes

FIGURE 4: Projection and correlation of impact-induced damage modes [20]

2.3 Modelling and computer simulation

2.3.1 Three-dimensional stresses from two-dimensional formulation

One of the key limitations of the Classical Lamination Theory is that each ply is assumed to be in plane stress forms, and inter-laminar associated with the z axis are neglected. As different Poisson's ratios undergo different transverse deformations which tend to expand the 0^0 layer and compress the 90^0 layer that generate stresses in z axis that can cause failure in the form of de-laminations or separation of the laminae. Stresses in a laminate vary from layer to layer. Equivalent system of forces and moments acting on a laminate cross section can be obtained by integrating the corresponding stresses through the laminate thickness h with respect to the mid-plane. The constitutive-relations for multilayer orthotropic plate could be obtained from a general case of n-ply panel. A schematic of symmetric 8-ply panel $[\pm 45^0/0^0/90^0]_S$ is shown in **FIGURE 5**.

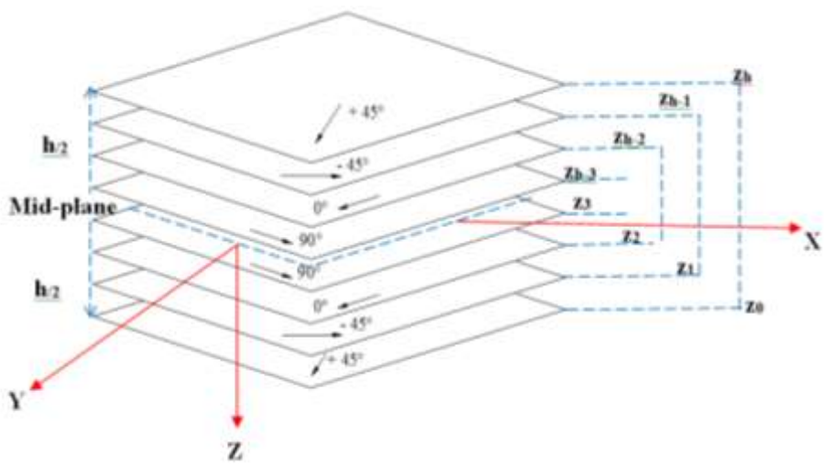

FIGURE 5: Coordinate locations of ply in a laminate

The panel has thickness $h = \sum_{k=1}^{n} t_k$, each ply has a thickness t_k, subscript k indicates layer number, and location of its mid-plane is h/2 from top or bottom surface. Coordinates of each ply surface from top to bottom are given as follows:

$h_0 = -\frac{h}{2}$(top surface), $h_1 = -\frac{h}{2} + t_1$(bottom surface); for Ply k: $(k = 2, 3, \cdots, n-2, n-1)$

$h_{k-1} = -\frac{h}{2} + \sum_{=1}^{k-1} t$ (top), $h_k = -\frac{h}{2} + \sum_{=1}^{k} t$ (bottom); Ply n: $h_{n-1} = \frac{h}{2} - t_n$(top surface), $h_n = \frac{h}{2}$(bottom surface); $\bar{z}_k = \frac{h_{k-1}+h_k}{2}$ coordinate of mid-surface of k^{th} layer.

To obtain force and moment resultants form a statically equivalent system that does not express z-coordinate explicitly among $[Q_{ij}]$, [T], and [R] matrices that yield components of fourth-order tensors transformed reduced coefficients' $[\bar{Q}_{ij}]$, and compliance $[\bar{S}_{ij}]$ matrices please refer to [1],[3], and [1]. The force-moment system acting on the mid-plane can thus be obtained by replacing continuous integral with summation of integrals for contribution from each layer:

$$\begin{Bmatrix} N_x \\ N_y \\ N_{xy} \end{Bmatrix} = \int_{-h/2}^{h/2} \begin{Bmatrix} \sigma_x \\ \sigma_x \\ \tau_{xy} \end{Bmatrix} dz = \sum_{k=1}^{n} \int_{h_{k-1}}^{h_k} \begin{Bmatrix} \sigma_x \\ \sigma_x \\ \tau_{xy} \end{Bmatrix} dz \qquad (1)$$

and

$$\begin{Bmatrix} M_x \\ M_y \\ M_{xy} \end{Bmatrix} = \int_{-h/2}^{h/2} \begin{Bmatrix} \sigma_x \\ \sigma_x \\ \tau_{xy} \end{Bmatrix} z dz = \sum_{k=1}^{n} \int_{h_{k-1}}^{h_k} \begin{Bmatrix} \sigma_x \\ \sigma_x \\ \tau_{xy} \end{Bmatrix} z dz \qquad (2)$$

The stresses in Eqs (1), (2) can be related directly to the mid-plane strains and plate curvatures that give

$$\begin{Bmatrix} N_x \\ N_y \\ N_{xy} \end{Bmatrix} = \sum_{k=1}^{n} \left\{ \int_{h_{k-1}}^{h_k} \begin{bmatrix} \bar{Q}_{11} & \bar{Q}_{12} & \bar{Q}_{16} \\ \bar{Q}_{12} & \bar{Q}_{22} & \bar{Q}_{26} \\ \bar{Q}_{16} & \bar{Q}_{26} & \bar{Q}_{66} \end{bmatrix}_k \begin{Bmatrix} \varepsilon_x^0 \\ \varepsilon_y^0 \\ \gamma_{xy}^0 \end{Bmatrix} dz + \int_{h_{k-1}}^{h_k} \begin{bmatrix} \bar{Q}_{11} & \bar{Q}_{12} & \bar{Q}_{16} \\ \bar{Q}_{12} & \bar{Q}_{22} & \bar{Q}_{26} \\ \bar{Q}_{16} & \bar{Q}_{26} & \bar{Q}_{66} \end{bmatrix}_k \begin{Bmatrix} k_x \\ k_y \\ k_{xy} \end{Bmatrix} z dz \right\} \qquad (3)$$

$$\begin{Bmatrix} M_x \\ M_y \\ M_{xy} \end{Bmatrix} = \sum_{k=1}^{n} \left\{ \int_{h_{k-1}}^{h_k} \begin{bmatrix} \bar{Q}_{11} & \bar{Q}_{12} & \bar{Q}_{16} \\ \bar{Q}_{12} & \bar{Q}_{22} & \bar{Q}_{26} \\ \bar{Q}_{16} & \bar{Q}_{26} & \bar{Q}_{66} \end{bmatrix}_k \begin{Bmatrix} \varepsilon_x^0 \\ \varepsilon_y^0 \\ \gamma_{xy}^0 \end{Bmatrix} z dz + \int_{h_{k-1}}^{h_k} \begin{bmatrix} \bar{Q}_{11} & \bar{Q}_{12} & \bar{Q}_{16} \\ \bar{Q}_{12} & \bar{Q}_{22} & \bar{Q}_{26} \\ \bar{Q}_{16} & \bar{Q}_{26} & \bar{Q}_{66} \end{bmatrix}_k \begin{Bmatrix} k_x \\ k_y \\ k_{xy} \end{Bmatrix} z^2 dz \right\} \qquad (4)$$

Since mid-plane strains and plate curvatures remain constant not only within a lamina but also for all the laminae that can be taken outside the summation sign. Thus, the equations become

$$\begin{Bmatrix} N_x \\ N_y \\ N_{xy} \end{Bmatrix} = \sum_{k=1}^{n} \left[\begin{bmatrix} \bar{Q}_{11} & \bar{Q}_{12} & \bar{Q}_{16} \\ \bar{Q}_{12} & \bar{Q}_{22} & \bar{Q}_{26} \\ \bar{Q}_{16} & \bar{Q}_{26} & \bar{Q}_{66} \end{bmatrix}_k \int_{h_{k-1}}^{h_k} dz \right] \begin{Bmatrix} \varepsilon_x^0 \\ \varepsilon_y^0 \\ \gamma_{xy}^0 \end{Bmatrix} + \left[\sum_{k=1}^{n} \begin{bmatrix} \bar{Q}_{11} & \bar{Q}_{12} & \bar{Q}_{16} \\ \bar{Q}_{12} & \bar{Q}_{22} & \bar{Q}_{26} \\ \bar{Q}_{16} & \bar{Q}_{26} & \bar{Q}_{66} \end{bmatrix} \int_{h_{k-1}}^{h_k} z dz \right] \begin{Bmatrix} k_x \\ k_y \\ k_{xy} \end{Bmatrix}_k \qquad (5)$$

$$\begin{Bmatrix} M_x \\ M_y \\ M_{xy} \end{Bmatrix} = \sum_{k=1}^{n} \left[\begin{bmatrix} \bar{Q}_{11} & \bar{Q}_{12} & \bar{Q}_{16} \\ \bar{Q}_{12} & \bar{Q}_{22} & \bar{Q}_{26} \\ \bar{Q}_{16} & \bar{Q}_{26} & \bar{Q}_{66} \end{bmatrix}_k \int_{h_{k-1}}^{h_k} z dz \right] \begin{Bmatrix} \varepsilon_x^0 \\ \varepsilon_y^0 \\ \gamma_{xy}^0 \end{Bmatrix} + \left[\sum_{k=1}^{n} \begin{bmatrix} \bar{Q}_{11} & \bar{Q}_{12} & \bar{Q}_{16} \\ \bar{Q}_{12} & \bar{Q}_{22} & \bar{Q}_{26} \\ \bar{Q}_{16} & \bar{Q}_{26} & \bar{Q}_{66} \end{bmatrix} \int_{h_{k-1}}^{h_k} z^2 dz \right] \begin{Bmatrix} k_x \\ k_y \\ k_{xy} \end{Bmatrix}_k \qquad (6)$$

For three-dimensional panels, constructed by stacking several unidirectional laminae in a specified sequence of orientation, transformation of equations can be extended and written in simple component forms:

$$\begin{bmatrix} N_{xx} \\ N_{yy} \\ N_{xy} \end{bmatrix}_k = \begin{bmatrix} A_{11} & A_{12} & A_{16} \\ A_{12} & A_{22} & A_{26} \\ A_{16} & A_{26} & A_{66} \end{bmatrix}_k \begin{Bmatrix} \varepsilon_{xx}^0 \\ \varepsilon_{yy}^0 \\ \gamma_{xy}^0 \end{Bmatrix}_k + \begin{bmatrix} B_{11} & B_{12} & B_{16} \\ B_{12} & B_{22} & B_{26} \\ B_{16} & B_{26} & B_{66} \end{bmatrix}_k \begin{Bmatrix} k_{xx} \\ k_{yy} \\ k_{xy} \end{Bmatrix}_k$$

$$\begin{bmatrix} M_{xx} \\ M_{yy} \\ M_{xy} \end{bmatrix}_k = \begin{bmatrix} B_{11} & B_{12} & B_{16} \\ B_{12} & B_{22} & B_{26} \\ B_{16} & B_{26} & B_{66} \end{bmatrix}_k \begin{Bmatrix} \varepsilon_{xx}^0 \\ \varepsilon_{yy}^0 \\ \gamma_{xy}^0 \end{Bmatrix}_k + \begin{bmatrix} D & D_{12} & D_{16} \\ D_{12} & D_{22} & D_{26} \\ D_{16} & D_{26} & D_{66} \end{bmatrix}_k \begin{Bmatrix} k_{xx} \\ k_{yy} \\ k_{xy} \end{Bmatrix}_k \qquad (8)$$

The components of out-of-plane shear forces may be written as

$$\begin{Bmatrix} Q_y \\ Q_x \end{Bmatrix}_k = \begin{bmatrix} H_{44} & H_{45} \\ H_{45} & H_{55} \end{bmatrix}_k \begin{Bmatrix} \gamma_{yz} \\ \gamma_{xz} \end{Bmatrix}_k \qquad (9)$$

Whereas: A_{ij} (extensional stiffness), B_{ij} (bending-extension coupling), D_{ij} (bending stiffness), and H_{ij} is (inter-laminar shear stiffness coefficients).

To formulate three dimensional stresses from integration of two-dimensional stresses the following simplifications: no effects from extension-bending coupling matrix $[B_{ij} = 0]$ because of symmetric panels, neglect of inter-laminar compressive stresses matrix $[H_{ij} = 0]$, and loading in lateral directions were neglected.

The mismatch of Poisson ratios and effects of shear coupling and generate inter-laminar stresses in z-direction that tend to slide one ply over adjacent ones. Equilibrium equations similar to three-dimensional elasticity solution [20] need to be derived. As Poisson's ratio in terms of through-thickness and in-plane strain in the direction of applied load can be written as

$$\nu_{xz} = -\frac{\varepsilon_{xx}}{\varepsilon_{zz}} \qquad (10)$$

With all forces and moments zero except the loading Nx ≠ 0, through-thickness strain can be written in terms of the total change in thickness dh divided by the average laminate thickness h:

$$\varepsilon_{zz} = \frac{dh}{h} \qquad (11)$$

The total thickness change can be written as follows:

$$dh = \int_{-h}^{h} \varepsilon_{zz} dz \qquad (12)$$

Uniform stresses in each layer can be determined from the Hooke's law. The through-thickness strains from elements of the compliance matrix $[\bar{S}]$ in any k^{th} layer give

$$\varepsilon_{xx} = \bar{S}_{11}\sigma_{xx} + \bar{S}_{12}\sigma_{yy} + \bar{S}_{13}\sigma_{zz} + \bar{S}_{16}\tau_{xy}$$

$$\varepsilon_{yy} = \bar{S}_{12}\sigma_{xx} + \bar{S}_{22}\sigma_{yy} + \bar{S}_{23}\sigma_{zz} + \bar{S}_{26}\tau_{xy}$$

$$\boldsymbol{\varepsilon_{zz} = \bar{S}_{13}\sigma_{xx} + \bar{S}_{23}\sigma_{yy} + \bar{S}_{s3}\sigma_{zz} + \bar{S}_{36}\tau_{xy}}$$

$$\boldsymbol{\gamma_{yz} = \bar{S}_{44}\tau_{yz} + \bar{S}_{45}\tau_{zx}}$$

$$\boldsymbol{\gamma_{xz} = \bar{S}_{45}\tau_{yz} + \bar{S}_{55}\tau_{zx}}$$

$$\boldsymbol{\gamma_{xy} = \bar{S}_{16}\sigma_{x} + \bar{S}_{26}\sigma_{y} + +\bar{S}_{36}\sigma_{zz} + +\bar{S}_{66}\tau_{xy}}$$

$$\boldsymbol{\varepsilon^{k}_{zz} = \bar{S}^{k}_{13}\sigma^{k}_{xx} + \bar{S}^{k}_{23}\sigma^{k}_{yy} + \bar{S}^{k}_{33}\tau^{k}_{xy}} \qquad \textbf{(13)}$$

Simplified in-plane constitutive equations for the k[th] layer can be obtained from Eq. (13):

$$\begin{Bmatrix}\sigma_{xx}\\ \sigma_{yy}\\ \tau_{xy}\end{Bmatrix}_k = \begin{bmatrix}\bar{Q}_{11} & \bar{Q}_{12} & \bar{Q}_{16}\\ \bar{Q}_{21} & \bar{Q}_{22} & \bar{Q}_{26}\\ \bar{Q}_{16} & \bar{Q}_{26} & \bar{Q}_{66}\end{bmatrix}_k \begin{Bmatrix}\varepsilon_{xx}\\ \varepsilon_{yy}\\ \gamma_{xy}\end{Bmatrix}_k \qquad \textbf{(14)}$$

For a symmetric laminate under in-plane loading; Nx ≠ 0, strains in the k[th] layer are:

$$\begin{Bmatrix}\varepsilon_{xx}\\ \varepsilon_{yy}\\ \gamma_{xy}\end{Bmatrix}_k = \begin{Bmatrix}\varepsilon^0_{xx}\\ \varepsilon^0_{yy}\\ \gamma^0_{xy}\end{Bmatrix}_k = [A]^{-1}\begin{Bmatrix}N_{xx}\\ 0\\ 0\end{Bmatrix}_k \qquad \textbf{(15)}$$

Combining Eqs (14)-(15) give

$$\begin{Bmatrix}\sigma_{xx}\\ \sigma_{yy}\\ \tau_{xy}\end{Bmatrix}_k = \begin{bmatrix}\bar{Q}_{11} & \bar{Q}_{12} & \bar{Q}_{16}\\ \bar{Q}_{21} & \bar{Q}_{22} & \bar{Q}_{26}\\ \bar{Q}_{16} & \bar{Q}_{26} & \bar{Q}_{66}\end{bmatrix}_k \begin{Bmatrix}A^{-1}_{11}\\ A^{-1}_{12}\\ A^{-1}_{16}\end{Bmatrix}_k N_{xx} \qquad \textbf{(16)}$$

Putting back in Eq(13), it gives through-thickness strains in the k[th] layer:

$$\boldsymbol{\varepsilon^{k}_{zz} = N_x\left[\begin{matrix}A^{-1}_{11}\left(\bar{S}^{k}_{13}\bar{Q}^{k}_{11} + \bar{S}^{k}_{23}\bar{Q}^{k}_{12} + \bar{S}^{k}_{36}\bar{Q}^{k}_{16}\right) + A^{-1}_{12}\left(\bar{S}^{k}_{13}\bar{Q}^{k}_{12} + \bar{S}^{k}_{23}\bar{Q}^{k}_{22} + \bar{S}^{k}_{36}\bar{Q}^{k}_{26}\right)\\ +A^{-1}_{16}\left(\bar{S}^{k}_{13}\bar{Q}^{k}_{16} + \bar{S}^{k}_{23}\bar{Q}^{k}_{26} + \bar{S}^{k}_{36}\bar{Q}^{k}_{66}\right)\end{matrix}\right]} \qquad \textbf{(17)}$$

All terms are known and constant within any layer of a given symmetric laminate. Thus Eq. (17) can be used to obtain total change in laminate thickness:

$$\boldsymbol{dh = N_x(A^{-1}_{11}F_1 + A^{-1}_{12}F_2 + A^{-1}_{16}F_6)} \qquad \textbf{(18)}$$

Where Fi are defined as

$$\boldsymbol{F_i = \sum_{k=1}^{N}\left[\left(\bar{S}^{k}_{13}\bar{Q}^{k}_{16} + \bar{S}^{k}_{23}\bar{Q}^{k}_{26} + \bar{S}^{k}_{36}\bar{Q}^{k}_{66}\right)_{t_k}\right](i = 1, 2, 5)} \qquad \textbf{(19)}$$

The Eq (19) gives through-thickness Poisson's ratios as

$$\boldsymbol{\nu_{xz} = -\frac{A^{-1}_{1i}F_i}{hA^{-1}_{11}}(i = 1, 2, 6),\ or\ \nu_{xz} = \frac{(A^{-1}_{11}F_1 + A^{-1}_{12}F_2 + A^{-1}_{16}F_6)}{hA^{-1}_{11}}} \qquad \textbf{(20)}$$

In a similar fashion, it can be shown that the υ_{yz} for loading in the y-direction is

$$\boldsymbol{\nu_{yz} = -\frac{A^{-1}_{2i}F_i}{hA^{-1}_{22}}(i = 1, 2, 6)} \qquad \textbf{(21)}$$

The inter-laminar stresses can be obtained using the three stress equilibrium equations [3],[1]. The ply-by-ply in-plane stresses are integrated through-thickness to determine inter-laminar transverse shear stresses from the equilibrium equations:

$$\boldsymbol{\tau_{xz} = \sum_{k=1}^{N}\int_{z_{k-1}}^{z_k}\left(\frac{\partial\sigma_{xx}}{\partial x} + \frac{\partial\tau_{xy}}{\partial y}\right)dz} \qquad \textbf{(22)}$$

and

$$\boldsymbol{\tau_{yz} = \sum_{k=1}^{N}\int_{z_{k-1}}^{z_k}\left(\frac{\partial\sigma_{yy}}{\partial y} + \frac{\partial\tau_{xy}}{\partial x}\right)dz} \qquad \textbf{(23)}$$

Since drop-weight impacts generate compressive stresses, and out-of-plane normal strains do not contribute and de-lamination failure modes. Thus components of strains can be neglected from compliance matrix that gives simplified relations.

$$\boldsymbol{\left\{S_{i=1,6;\ j=1,6}\right\} = \begin{bmatrix}\frac{1}{E_1} & -\frac{\nu_{21}}{E_2} & -\frac{\nu_{31}}{E_3} & 0 & 0 & 0\\ -\frac{\nu_{12}}{E_1} & \frac{1}{E_2} & -\frac{\nu_{32}}{E_3} & 0 & 0 & 0\\ -\frac{\nu_{13}}{E_1} & -\frac{\nu_{23}}{E_2} & \frac{1}{E_3} & 0 & 0 & 0\\ 0 & 0 & 0 & \frac{1}{G_{23}} & 0 & 0\\ 0 & 0 & 0 & 0 & \frac{1}{G_{31}} & 0\\ 0 & 0 & 0 & 0 & 0 & \frac{1}{G_{12}}\end{bmatrix}} \qquad \textbf{(24)}$$

thus

$$\boldsymbol{S = S_{11}S_{22}S_{23} - S_{11}S^2_{23} - S_{22}S^2_{13} - S_{33}S^2_{12} + 2S_{12}S_{23}S_{13}}$$

The transverse normal strain for the orthotropic stress-strain relations can be obtain as

$$\boldsymbol{\varepsilon_{zz} = \frac{1}{C_{33}}\left(\sigma_{zz} - C_{13}\varepsilon_{xz} - C_{23}\varepsilon_{yz}\right)} \qquad \textbf{(25)}$$

that can be used to eliminate $\boldsymbol{\varepsilon_{zz}}$ from the stress-strain relations for the k[th] layer, leaving

$$\begin{bmatrix}\sigma_{xx}\\ \sigma_{yy}\\ \tau_{yz}\\ \tau_{xz}\\ \tau_{xy}\end{bmatrix}_k = \begin{bmatrix}Q_{11} & Q_{12} & 0 & 0 & 0\\ Q_{21} & Q_{22} & 0 & 0 & 0\\ 0 & 0 & Q_{44} & 0 & 0\\ 0 & 0 & 0 & Q_{55} & 0\\ 0 & 0 & 0 & 0 & Q_{66}\end{bmatrix}_k \begin{bmatrix}\varepsilon_{xx}\\ \varepsilon_{yy}\\ \gamma_{yz}\\ \gamma_{xz}\\ \gamma_{xy}\end{bmatrix}_k \qquad \textbf{(26)}$$

If σ_{zz} is neglected, the coefficients of reduced stiffness matrix can be obtained as

$$\boldsymbol{Q_{ij} = \begin{bmatrix}C_{ij} - \frac{C_{i3}C_{j3}}{C_{33}}, if\ i, j = 1, 2\\ C_{ij,}\quad \textbf{if } i, j = 4, 5, 6\end{bmatrix}}$$

Whereas: $\boldsymbol{C_{11} = \frac{S_{22}S_{33} - S^2_{23}}{S}, C_{12} = \frac{S_{13}S_{23} - S_{12}S_{33}}{S}, C_{13} = \frac{S_{12}S_{23} - S_{13}S_{22}}{S}}$

$\boldsymbol{C_{22} = \frac{S_{11}S_{33} - S^2_{13}}{S}, C_{23} = \frac{S_{12}S_{13} - S_{23}S_{11}}{S}, C_{33} = \frac{S_{11}S_{22} - S^2_{12}}{S},}$ $\boldsymbol{C_{44} = \frac{1}{S_{44}}, C_{55} = \frac{1}{S_{55}}, C_{66} = \frac{1}{S_{66}}}$

Since most of the failure criteria require stress allowable in terms of ply local coordinates. Therefore, stresses in global coordinates for any ply can be transformed into local ply coordinates. Subscripts correspond to fibre direction of the ply, distinguish, and separate the failure modes as follows:

$$\boldsymbol{\begin{Bmatrix}\tau_{13}\\ \tau_{23}\end{Bmatrix}_k = \begin{bmatrix}\cos\theta & \sin\theta\\ -\sin\theta & \cos\theta\end{bmatrix}_k \begin{Bmatrix}\tau_{xz}\\ \tau_{yz}\end{Bmatrix}_k} \qquad \textbf{(27)}$$

The simplified solution returns ply-level shear stresses at any point as shown in global laminate coordinates **FIGURE 6**.

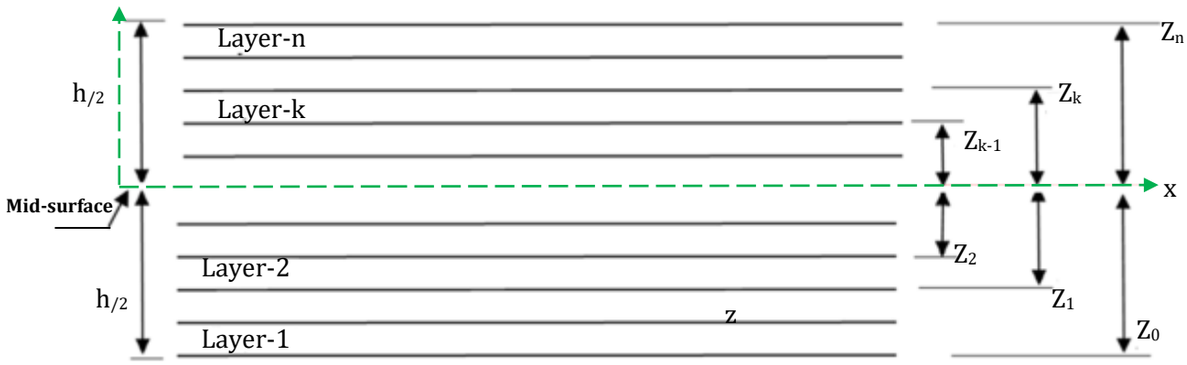

FIGURE 6: Coordinate system and layer positions defined in a laminate

Where θ is the ply angle (between the fibre direction and the global x-direction), k denotes relevant ply number, and N denotes total number of plies in a laminate.

2.3.2 Efficient prediction of three-dimensional stress from damaged region

The formulation of three-dimensional stresses based on neglecting the derivatives of in-plane forces and twisting moments, and mixed derivatives of the bending moments with respect to in-plane coordinates is detailed in **Section**2.3.1 above. Simulation generated two-dimensional in-plane normal and shear stress values are selected from high stress gradient regions under impactor nose tips. The stresses are utilized by the descritised equilibrium Eqs (22)-(23) with forward differencing scheme. The method efficiently predicts 3-D transverse shear stresses from numerical integration of in-plane stresses using modified Simpson's rule based on second-order polynomial [20], [35]. The descritised equations are then numerically integrated with the modified Simpson's rule to predict in-plane plane and out-of-plane stresses equivalent to three-dimensional model. Additional efficient aspects of adaptive meshing to partitioned domain under impactor nose-tips were also incorporated in simulation models to obtain more reliable prediction stress quantities.

2.3.2.1 Adaptive meshing schemes

The grid adaptation procedure called adaptive meshing yields an acceptable accuracy with the minimum amount of computational efforts [20]. The technique is highly useful for adaptation of various discontinuities, interfaces, or localized larger stress gradient regions. Several approaches have been employed for both structured and non-structured mesh adaptation categorized into h-methods and p-methods. The h-methods control the mesh size in the finite element grid by subdividing the elements when the local error estimate exceeds a user-defined tolerance. The p-methods adapt the approximation by increasing or decreasing the local error of polynomial basis elements where the error in the element exceeds or falls below user-defined error criterion. Combination of the adaptive strategies that leads to effective h-p method is selected to combine variation in local mesh size for better theoretical convergence rate.

2.3.2.2 Domain partitioning

The damaged areas need to be partitioned to create dense elements in damaged areas and course elements in un-damaged areas using adaptive meshing techniques. Surfaces of the panels slightly larger than the areas under impactor nose-tips are virtually partitioned to apply adaptive meshing techniques that create fine meshes in the areas. The smaller elements allow better simulation of stress distributions at the mesh-transition regions to reliably predict damage initiation loads. In regions away of the impact zone where damage is not expected to occur or its initiation load is not critical course meshes get created. The adaptive meshing techniques are incorporated in the library of ABAQUS software. Thus adaptive meshing was implemented for un-structured grids using local refinement frequency of sweeping ratios of grids. The program can start with a course initial mesh and compute the field on it. Mesh can be refined based on the first coarse approximations of the field automatically.

2.3.2.3 Developing simulation models

Simulation models in publication [34] were selected and adopted for present study. Modification of domain partitioning and change in built-in to mode-base failure criteria were incorporated in the models. Schematics of symmetric panel and impact affected area in **FIGURE 1**, impact machine and impactors in **FIGURE 2** and material properties are given in **TABLE 1**. Both the impactors were meshed with fully integrated continuum 8-node C3D8 three-dimensional (3D) linear hexahedral 708 elements. Panels in Model 1 were meshed with general purpose linear fully integrated quadrilateral conventional shell (S4) 234 elements and also with reduced integration triangular conventional shell (S3R) 621 elements using two different levels of refinement. Each laminate ply is modeled with deformable one shell element through-the-thickness which behaves according to the

continuum damage model. Panels in Model 2 were meshed with adaptive meshing implemented for un-structured grids using local refinement frequency of sweeping ratios of 10:3, 20:3, and 30:3 grids. The **FIGURE 7**shows simulation generated meshed by S4 elements domains under impactor nose-tips, ply-by-ply, and panels with increasing number from 234 to 922, 2130, up to 3411.

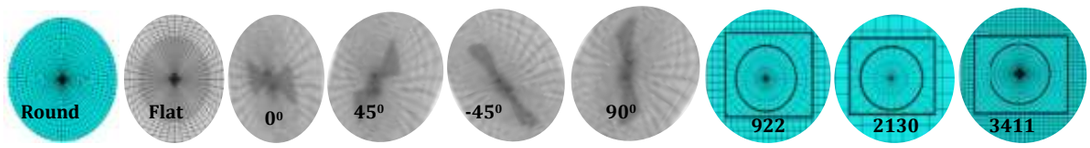

a) **b)** **c)**

FIGURE 7: Adaptive meshed a) Partitioned domains, b) Angle plies, and c) Panels

Simulation generated images of Model 1 consisting of un-partitioned domain under impactor nose-tips in **FIGURE 8(a),** Mode 2 consisting of partitioned domains under impactor nose-tips with adaptive meshing are depicted in **FIGURE 8(b).**

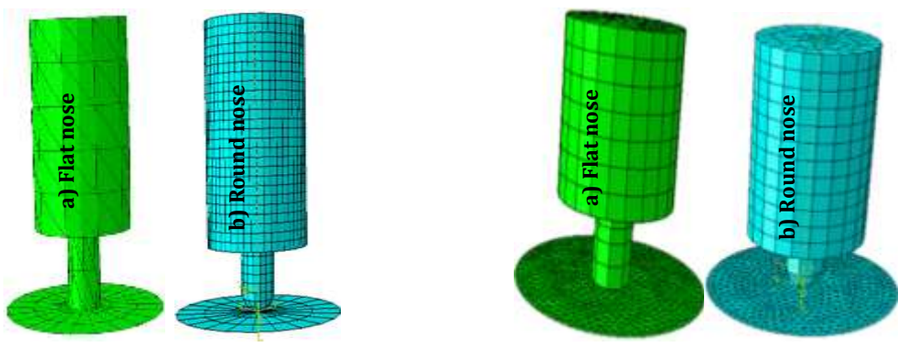

a) Model 1 **b) Model 2**

FIGURE 8: Computer generated images of flat and round nose impact models

3. Results and discussions of experimental testing

3.1 Damaged area and load/energy-time of 8-Ply panel with 2m/s velocity

Impact tested panels along with corresponding recorded quantities of displacement, velocity, energy, and force history are post-processed and analyzed to approximate impact-induced damage. Selected ones are being presented here with discussions. The **Figure 9(a) & (b)** depict scanned panels impacted by flat and round nose impactors, and damage areas projected to outer surface ply. Percentage ratios of damaged areas were predicted from MATLAB™ program in **TABLE 2**. The impact area by flat nose impact approximates to 14% of the panel, while by round nose it approximate to 8%. The predicted ratios indicate larger surface damage by flat nose impactor than the round nose one. This is due to larger global elastic-deflection and absorbed energy proportions to projected surface damage areas reported in [20].

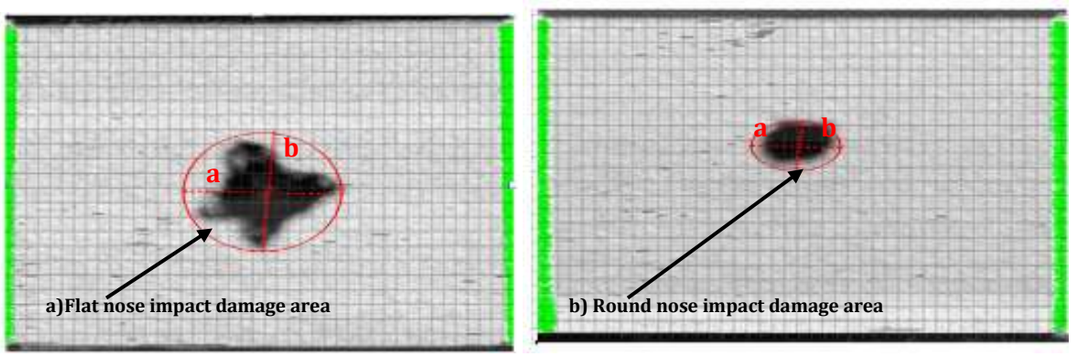

FIGURE 9: Ratios of damage area to impacted panel

The **FIGURE 10(a)** shows comparison of **FIGURE 4** typical load/energy-time history curves (the bending stiffness). The curve goes fairly smooth during ascending section of loading until reaching the maximum load or peak force until a sudden drop in load drops to 8.kN, a dip in loading corresponds to initial damage that onset to propagate matrix-cracking, fibre-breakage, or de-lamination. During unloading section, the curve continues reduction in load up to zero level until end of the impact event. The energy-time curve illustrates steady increase until the highest tip of the curve shows maximum impact energy 24J. The resulting plateau in the energy-time curve represents the energy absorbed by the composite panels,

primarily dissipated through the creation of damage [5]. Then curve decreases to 15J that indicates transfer of impact energy into elastic energy that remains stable indicating complete absorption of impact energy until end of the event. The absorbed is used for rebound of the impactor. The elastic energy region in the curve could be approximated from ratio of elastic-energy/impact-energy [20], similarly from the same figure$\left(\frac{9}{25} * 100\right) \cong 36\%$. This indicates a severe local damage that can be attributed to ply-level failure. The curve continues following the constant path that can be attributed to absorption of all the impact energy approximated to$\left(\frac{16}{25} * 100\right) \cong 64\%$. The **FIGURE 10(b)** shows comparison of **FIGURE 4** flat-nose impacts. Its curve goes fairly smooth until a sudden drop in load (called threshold load) drops from 8.5kN and drops to 5.5kN indicating onset of ply level failure crack, occurrence of de-lamination, or perforation on the impacted side of panels [20]. During unloading section, it shows oscillations and increase in load after that point the curve follows steep descend it reaches zero at the end of the event. The flat-nose impact energy-time curve demonstrates increase without any reduction until it finally gets saturated. The curve does not show any oscillations or drops, but it follows the constant path that can be attributed to transformation of all the impact energy to absorbed energy. As impact energy is mainly absorb globally at ply-by-ply level fracture, matrix-cracks, de-bonding, de-lamination, plastic deformation, and the material damping due to the effect of the inter-laminar slippage. The panels absorbed all the impact energy, as impact energy curve increased until the end point of the test, and the curve illustrates the absorbed energy over time with no obvious difference under flat nose impact.

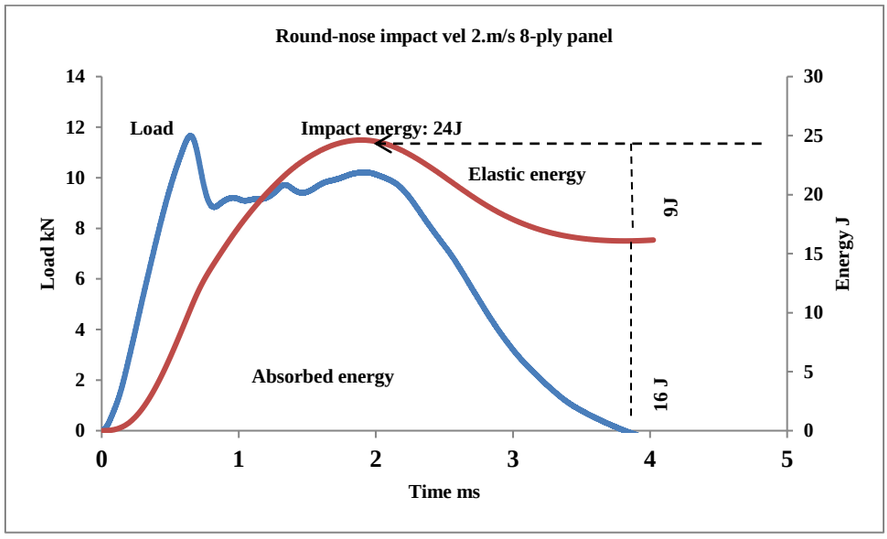

(a)

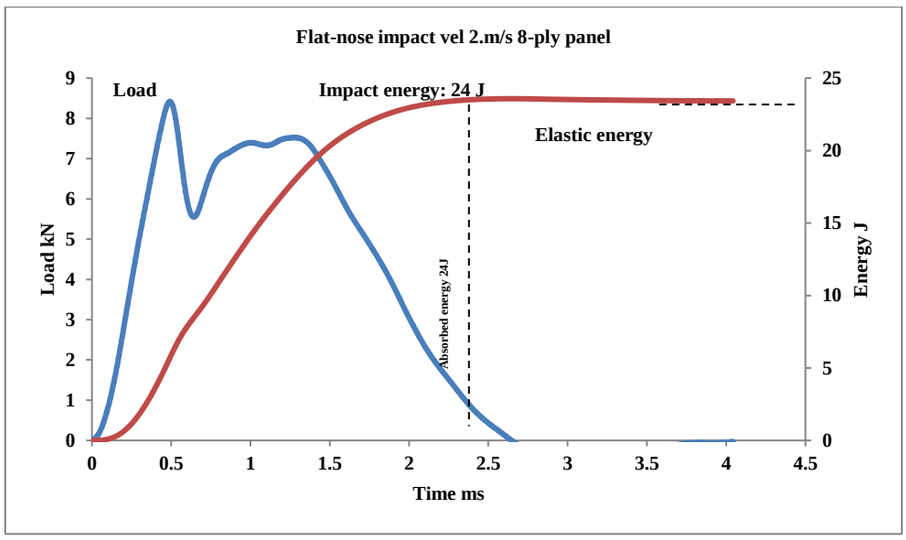

(b)

FIGURE 10: Load/energy-time curves of impacts on 8-ply-panels

3.2 Damaged area and Load/energy-time of 16-Ply panel with 3m/s velocity

Experimental tests of 16-ply panel at velocity 3m/s were performed according to the procedure outlined in [1]. The **Figure 11(a) & (b)** depicts scanned damage areas projected to outer surface ply from flat and round nose impacts. Percentage

ratios of damaged areas were predicted from MATLAB™ program in **TABLE 2**. The impact area by flat nose impact approximates to 16% of the panel, while by round nose it approximate to 10%. The predicted ratios indicate larger surface damage by flat nose impactor than the round nose one. This is due to larger global elastic-deflection and absorbed energy proportions to projected surface damage areas reported in [20].

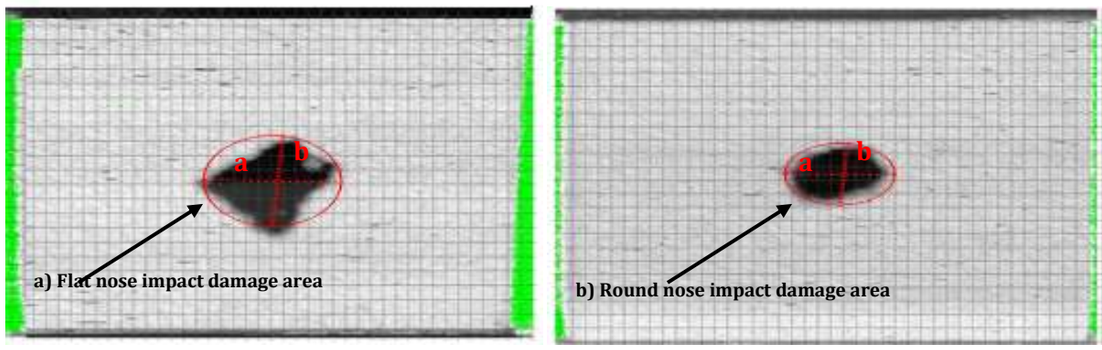

FIGURE 11: Ratios of damaged areas to impacted panels

The **FIGURE 12(a)** represents round-nose impacts of 16-ply panels at velocity 3.m/s. Its comparison to **FIGURE 4** loading part of the curve depicts sharp increase up to 17kN indicating elastic response with no damage. The round-nose curve takes turn and remains flat for the interval 1-1.2ms. This indicates contact loss between the impactor and the panel. During unloading section, the curve depicts a sudden load drop from 17kN to 12kN at 1.2ms that indicates ply level failure. After that point, the curve shows continuous reduction in load along with oscillations until the event ends at 2.9ms. The oscillations preceding first sudden load-drop reveal development of a crack, occurrence of de-lamination, or perforation on the impacted side of panels. The rebounding of the impactor is reproduced by the oscillations and then smooth reduction until the end of the impact events. The unloading part depicts high oscillations and break in round-nose curve indicating perforation or severe local damage to the panel. The resulting plateau in the round-nose impact energy-time curve represents the energy absorbed by the panel. Primarily energy dissipated through the creation of damage [34]. The curve illustrates steady increase until the highest tip of the curve shows maximum impact energy 26J at 1.5ms. After that point, the curve follows sharp decrease up to 9J that indicates phase transfer from impact energy to elastic energy. Then the curve continues its flat path until the impact even ends that indicates that all of the impact energy has been absorbed. The elastic energy zone remains almost stable that indicates complete absorption of the impact energy. The energy levels illustrate particularly the absorbed energy from the energy difference between maximum impact energy and elastic energy (used for rebound of the impactor). The elastic energy region in the figure could be approximated from ratio of elastic-energy 11J/impact-energy 35J as$\left(\frac{11}{35}*100\right)\cong 30\%$. This indicates a severe local damage (the puncture) that can be attributed to ply-level failure. The curve continues following the constant path that can be attributed to absorption of all the impact energy$\left(\frac{24}{35}*100\right)\cong 70\%$. The **FIGURE 12 (b)** represents flat-nose impacts of 16-ply panels at velocity 3.2m/s when compared to **FIGURE 4** curve goes fairly smooth during ascending section of loading until reaching the maximum load. No oscillations or load-drop can be observed. This implies that the panels still had good impact resistance capacity due to panels' inherent ply-based configurations. The load increases until it takes turn and remains flat between the interval range: 0.2-0.4ms. This indicates contact loss between the impactor and the panel. During unloading section, the curve depicts a sudden load drop from 17kN to 11kN at 0.6ms that indicates ply level failure. The rebounding of the impactor is reproduced by the oscillations and then smooth reduction until the end of the impact events. The unloading part depicts high oscillations and break due to the nose-shape of the impactor. This indicates matrix-cracking under the impact side or severe damage to the panel. The resulting plateau in the energy-time curve represents the energy absorbed by the composite panels, primarily dissipated through the creation of damage [20]. The flat-nose impact energy-time curve illustrates steady increase until the highest tip of the curve shows maximum impact energy 36J at 1.6ms. After that point, the curve follows sharp decrease up to 22J between the interval 1.6-2.9ms that indicates phase transfer from impact to elastic energy. Then the curve continues its flat path until the impact even ends that indicates that all of the impact energy has been absorbed. The elastic energy zone remains almost stable that indicates complete absorption of the impact energy until the end of the event. The energy levels particularly the absorbed energy from the energy difference between maximum impact energy and elastic energy (used for rebound of the impactor). The elastic energy region in the figure could be approximated from ratio of elastic-energy 11J/impact-energy 35J as$\left(\frac{14}{36}*100\right)\cong 30\%$. This could be correlated to a severe local damage (the puncture) that can be attributed to ply-level failure. The curve continues following the constant path that can be attributed to absorption of all the impact energy$\left(\frac{24}{35}*100\right)\cong 70\%$.

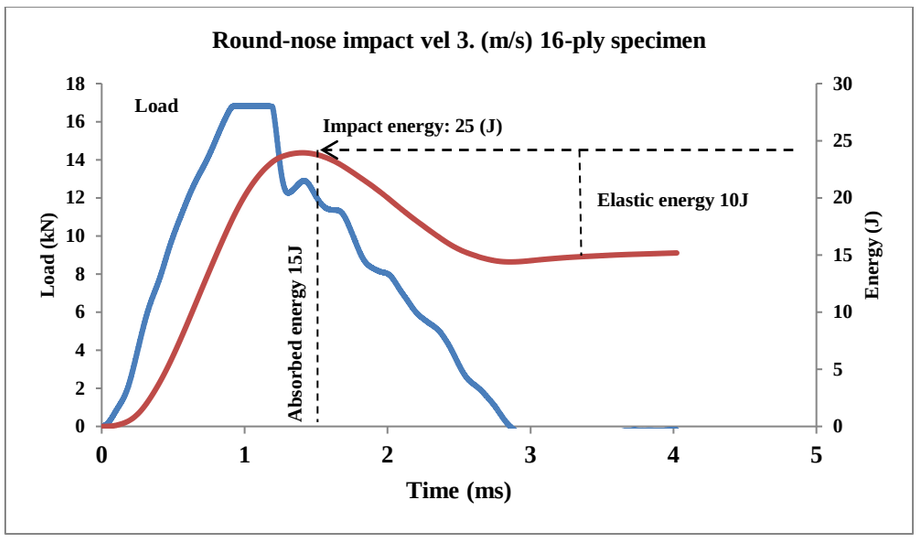

(a)

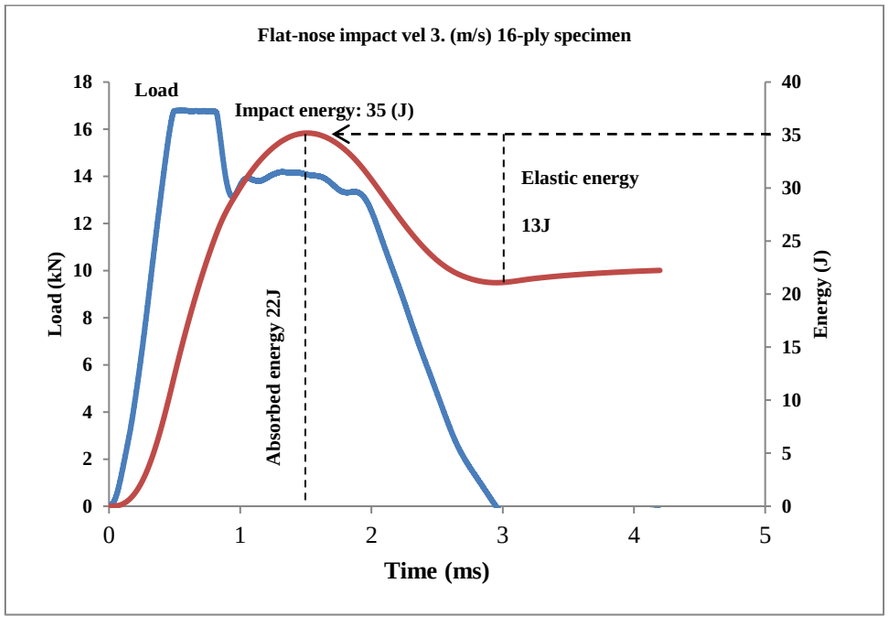

(b)

FIGURE 12: Load/energy-time curves: a) round, b) flat-nose impacts on 16-ply-panels

3.3 Damaged area and Load/energy-time of 24-Ply panel with 4.4m/s velocity

Experimental tests of 24-Ply panels at velocity 4.14m/s were performed according to the procedure outlined in [1]. The **Figure 13** depicts scanned damage areas projected to outer surface ply from flat and round nose impacts. Percentage ratios of damaged areas were predicted from MATLAB™ program in **TABLE 2**. The impact area by flat nose impact approximates to 22% of the panel, while by round nose it approximate to 16%. The predicted ratios indicate larger surface damage by flat nose impactor than the round nose one. This is due to larger global elastic-deflection and absorbed energy proportions to projected surface damage areas reported in [20].

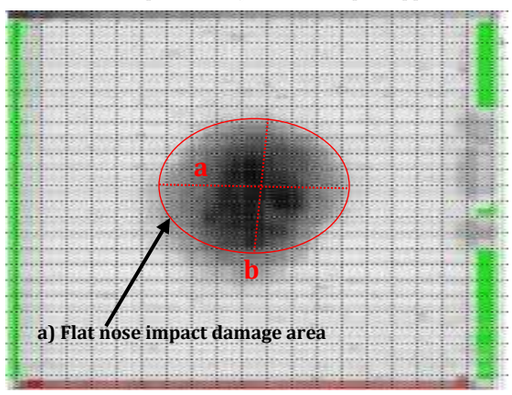

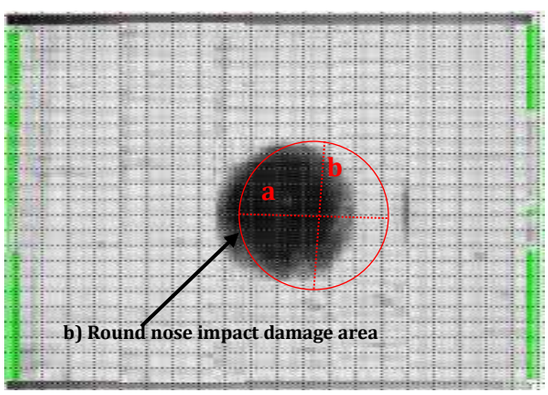

FIGURE 13: Ratios of damaged areas to impacted panels

The **FIGURE 14(a)** represents load/energy-time curves depict bulge at the impact point indicating matrix crack before steadily increasing up to 14kN in loading part at 0.3ms when compared to **FIGURE 4** round-nose impactor. At that point, a sudden drop can be seen in load up to 9kN that indicates a significant damage at the impact site to the panel most probably matrix crack or ply failure. After that point, the curve shows slight regain along with a few oscillations in load up to 12kN between the interval 0.3-2ms, and it continues with load reduction in load until the event ends at 3ms. The oscillations preceding first sudden load-drop reveal development of a crack, occurrence of de-lamination, or perforation on the impacted side of panels. The energy-time curve depicts that initial energy level remains constant until 0.2ms before it gains sharp increase up to 50J at 1.5ms. After that point, the curve follows the straight line path until the end of the impact event. This indicates absorption of all the impact energy. The energy-time curve depicts sharp increase in impact energy up to 41J at 1.6ms. After that point, the curve takes turn into straight line and follows the same flat path until the end of the impact event. A very few drops in the traces were observed, and heights of the drops were also relatively smaller. This indicates little de-lamination damage in the panel, and the main damage was caused matrix cracking. The panels are relatively thicker and could resist the impact, so absorbed all the impact energy, as impact energy curve increased until the test ends, and curve illustrates the absorbed energy over time with no obvious difference. The **FIGURE 14(b)** represents flat-nose impact load-time curve when compared to **FIGURE 4** that illustrates sharp increase during loading section of the curve until it reaches peak load 17kN at 0.2ms. The curve turns into straight line after that point and remains flat between 0.2-0.4ms. This indicates that contact between impactor and panel was lost. After that point, the curve starts steady decrease until the end of the impact event. This indicates that the impact could not inflict any major damage to the panel. This implies that the panel could still withstand the higher impact force with smaller central deformation. The energy-time curve depicts sharp increase in impact energy up to 41J at 1.6ms. At that point, the curve takes turn into straight line and follows the same flat path until the end of the impact event. A very few drops in the trace were observed as panels are relatively thicker could resist such impacts. The heights of the drops were relatively smaller indicating little de-lamination damage in the panel, and the main damage could cause by matrix cracking. The panels absorbed all the impact energy, as impact energy curve increased until the end point of the test, and the curve illustrates the absorbed energy over time with no obvious difference. Thus no predictions about comparison of the regions occupied by energy levels have been included.

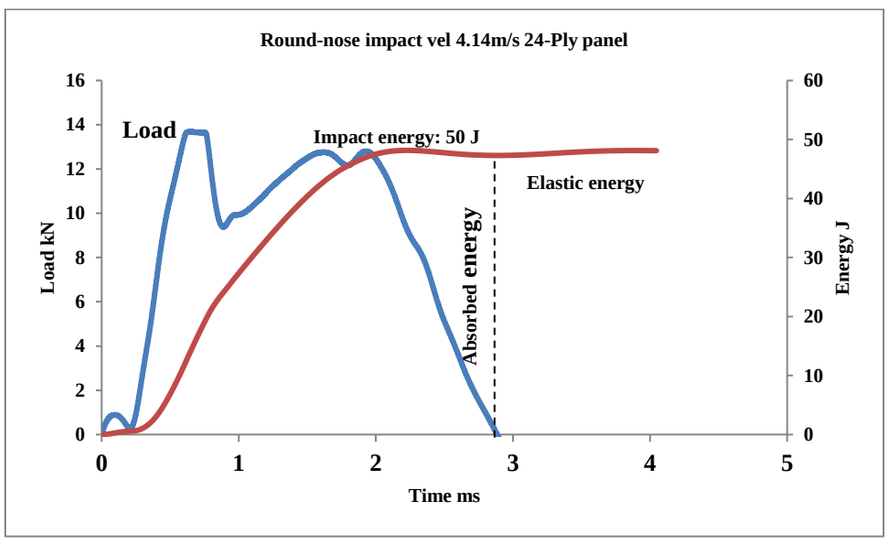

(a)

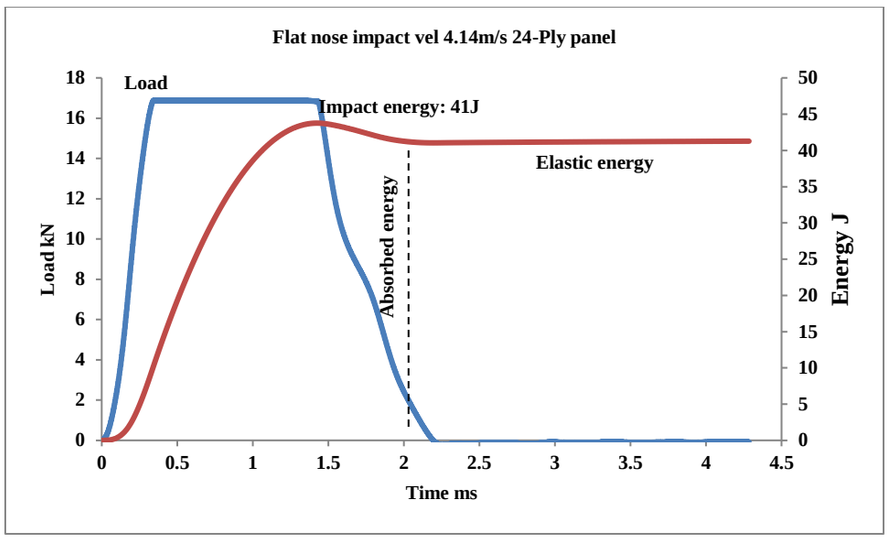

(b)

FIGURE 14: Load/energy-time curves of impacts on 24-ply-panels

3.4 Limitations of experimental studies

Examination of figure surface areas damage and comparison of curves demonstrate high level of consistency. As expected damage ratios increase in proportion to impactor nose-tips and panel thickness as shown in **Table 3**. Similarly peak load increases with growth of impact energy. The C-scanned images are useful to approximate size and depth of the first delamination encountered closet to the top ply, the first free surface reached by the ultrasonic waves. Such approximations provide knowledge about overall surface damage but not the size, shape or ply-by-ply damage. The amount of testing time and removal of functional aircraft part make it almost unpractical.

TABLE 3: Flat and round impact damage

Plies in panel	Impact-induced damage ratio (%)	
	Flat nose impact	Round nose impact
8	14	8.5
16	16	10
24	22	16

Data analyses plots maximum/peak load values under flat-nose impact curves matched well against the values available in the literature [20]. The load/energy-time history plots drop to 50% energy absorbed indicates energy levels correlation could particularly predict absorbed energy, while thin panel curves shown no elastic energy that indicates almost stable behaviour **Table 4**. In the case of round nose impact, high oscillations, severe load drop, and breaks in curves indicate potential contributions in perforation, severe local damage, or failure. furthermore, flat nose impact of 24-ply panel curves demonstrate traces of inconsistent behaviour where curves considerably turn into straight line without load drops.

TABLE 4: Comparison of flat and round nose impact energy forms

Plies in panel	Flat nose impact			Round nose impact		
	Impact energy	Elastic energy	Absorbed energy	Impact energy	Elastic energy	Absorbed energy
8	24	0	24	24	9	16
16	35	13	22	25	10	15
24	45	3	42	50	0	50

Performance evaluation of structural parts depends on damage location, pattern, and magnitude of internal damage embedded within the laminate: fibre-matrix debonding, matrix-cracks, and delamination. Moreover, information about detection and prediction of damage initiation, nature, progression, distribution, and progression so that expensive functional part suffered from no major damage be allowed usual function, repair/re-use or scrapped. Since experimental techniques lack in readily predicting ply level failure computer simulations were to supplement the analysis.

4. Discussions of simulated results

4.1 Three-dimensional stresses and mode-base failure criteria

The simulation generated in-plane normal and shear stress quantities from flat and round nose impacts were recorded at selected nodes of high stress gradient regions. The selected stresses were utilised in discretized equilibrium equation (22)–(23) for numerical integration through-the-thickness utilizing MATLAB™ program **TABLE 5** to compute three-dimensional (transverse shear stress) quantities.

TABLE 5: MATLAB™ program for prediction of three-dimensional stresses

```
Fprintf('================================================================================\n');

fprintf('||    Program to numerically integrate in-plane stresses to predict transverse shear stresses                ||\n');

fprintf('================================================================================\n\n');

ii=input['Enter no of plies in panel']% 8, 16, or 24 only;

% Select stresses from three nodes out of high-stress gradient region for forward differencing scheme to equilibrium equations

distance = input['Enter value']; % Distance between two nodal positions in axial direction; h=input['Enter value']; % half thickness of 2h thick ply;  disp('Enter stress values')

s11a =input('In-plane axial stresses at node 1'); s11b =('In-plane axial stresses at node 2);  multiple= (' multiplier of Simpson Rule = [1 4 2 --- 2 4 2 1'];%ii =i+j% i is multiplied by 2 and j is multiplied by 4. ; s11 = h*(s11b-s11a)/distance; for i = 3:2:23; s11(i)=2*s11(i);end% Simpson rule for odd multiples; for j =2:2:22; s11(j)=4*s11(j);end; % Simpson rule for even multiples;  s11f1 = s11;

 s12a = input['In-plane shear stresses at node 1']; s12b =('In-plane shear stresses at node 2); s12 = h*(s12b-s12a)/distance; for i = 3:2:23;s12(i)=2*s12(i); end % Integration for through-thickness in-plane shear stresses; for j =2:2:22;s12(j)=4*s12(j);end;  s12f1=s12;

distance = input('Distance between two nodal positions'); s22a=input('In-plane normal lateral stresses at node 1'); s22b = input('In-plane normal lateral stresses at node 3'); s22=h*(s22b-s22a)/distance; for i = 3:2:23;s22(i)=2*s22(i);end% Integration for through-thickness stresses in lateral direction; for j =2:2:22;s22(j)=4*s22(j);end;  s22f1=s22;  s21a = input('In-plane shear lateral stresses at node 1'); s21b = input('In-plane normal lateral stresses at node 3'); s21=h*(s21b-s21a/distance);for i = 3:2:23;s21(i)=2*s21(i);end % Integration for in-plane stresses in lateral direction; for j =2:2:22;s21(j)=4*s21(j);end; s21f1=s21; % for 24-Ply panel

diary stress_xx_yy.out; stress_xx_yy=fopen('stress_xx_yy.txt', 'w')

fprintf('======In-lane Normal Stresses======\n'); fprintf('Ply No      stress-xx     stres-yy \n');for ii= 1:24;sxx = s11f1;syy =  s22f1; fprintf('%2d \t\t%10.2e \t\t%10.2e\n',ii, sxx(ii),syy(ii));end; diary off;

diary stress_xy_yx.out; stress_xy_yx=fopen('stress_xy_yx.txt', 'w')

fprintf('=======In-plane Shear Stresses=====\n');fprintf('Ply No    stress-xy   stres-yx  \n')

 for ii= 1:24;sxy =  s12f1;syx =  s21f1; fprintf('%2d \t\t%10.2e \t\t%10.2e\n',ii, sxy(ii), syx(ii));end;

diary off;  diary stress_xz_yz.out stress_xz_yz=fopen('stress_xz_yz.txt', 'w')

 fprintf('====== Transverse Shear Stresses====\n'); fprintf('Ply No    stress-xz    stress-yz  \n');

 for ii=1:24;sxz = s11f1+s12f1;syz =s22f1+s21f1;  fprintf('%2d \t\t%10.2e \t\t%10.2e\n',ii, sxz(ii), syz(ii));end

 diary off
```

In [13], Hashin proposed three-dimensional failure criteria for unidirectional composites that use more than a single stress component to evaluate different failure modes. Failure indices of the criteria are related to fibre and matrix failures involved in four failure mode base criteria given in [18], [20]. When two interacting failure mechanisms are different, such as longitudinal failure and transverse failure, the quadratic criteria forces artificially smooth transition from one failure into the other. Therefore, separate in-plane and out-of-plane stresses based criteria were selected to predict failure against the strength parameters. Components of in-plane stresses based criteria produce fibre failure composed of normal, shear 'Fibre-Fracture Mode', and interaction between normal and shear result in 'Matrix-cracking (fibre-matrix de-bonding) Mode'. The components of transverse stresses ($\sigma_{13,}$ σ_{23}) coupling criteria delaminated plies is called `Quadratic Stress Criterion for De-lamination' coupling failure criteria [34] as shown in **Figure 15**.

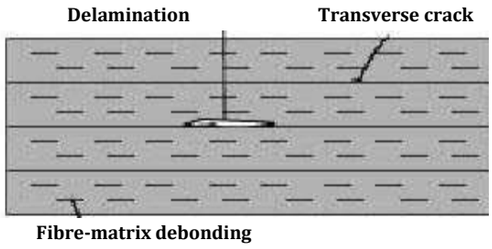

Figure 15: Ply-by-ply mode-base failure

Two interacting failure mechanisms are different as longitudinal and transverse failures, and quadratic criteria forces artificially smooth transition from one failure into the other. Therefore, separate in-plane and out-of-plane stresses based criteria were selected to predict failure against the strength parameters. Due to vertical drop-weight, equation (25) being compressive strain

$$\left(\frac{\sigma_{11}}{S_T}\right)^2 + \left(\frac{\tau_{12}}{S_{12}}\right)^2 \geq 1 \qquad (28)$$

$$\left(\frac{\sigma_{11}}{S_T}\right)^2 + \left(\frac{\tau_{12}}{S_{12}}\right)^2 \geq 1 \qquad (29)$$

The components of transverse stresses ($\sigma_{13,}$ σ_{23}) coupling criteria `Quadratic Stress Criterion for De-lamination':

formulation is neglected. We consider delamination failure criteria so normal transverse compressive stresses as derived in Eqs (24)-(27) are are also neglected ($\tau_{33} = 0$). The components of in-plane stresses based criteria produce fibre failure composed of normal (σ_1), shear (σ_{12}) 'Fibre-Fracture Mode':

interaction normal (σ_2), shear (σ_{12}) 'Matrix-cracking Mode':

$$\sqrt{\left(\frac{\tau_{13}}{S_{13}}\right)^2 + \left(\frac{\tau_{23}}{S_{23}}\right)^2} \geq 1 \qquad (30)$$

coupling failure criteria, implemented in MATLAB™ program to predict ply level damage and failure in **TABLE 6**.

TABLE 6: MATLAB™ program for ply-by-ply failure predictions

```
fprintf('================================================================================\n');

fprintf('||          MATLAB program to predict ply-by-ply failures using coupling failure criteria                ||\n');

fprintf('================================================================================\n\n');

%diary stress_xx_yy.out; stress_xx_yy=fopen('stress_xx_yy.txt', 'r')

fscanf('======In-lane Normal Stresses======\n'); fscanf('Ply No     stress-xx    stres-yy \n');for ii= 1:24;sxx = s11f1;syy =  s22f1; fscanf('%2d \t\t%10.2e \t\t%10.2e\n',ii, sxx(ii),syy(ii));end; %diary off;

%diary stress_xy_yx.out; stress_xy_yx=fopen('stress_xy_yx.txt', 'r')

fscanf('=======In-plane Shear Stresses=====\n');fscanf('Ply No     stress-xy   stres-yx  \n')

 for ii= 1:24;sxy =  s12f1;syx =  s21f1; fscanf('%2d \t\t%10.2e \t\t%10.2e\n',ii, sxy(ii), syx(ii));end%diary off

 %diary stress_xz_yz.out; stress_xz_yz=fopen('stress_xz_yz.txt', 'r')

 fscantf('====== Transverse Shear Stresses====\n'); fscanf('Ply No     stress-xz     stress-yz  \n');

 for ii=1:24;sxz = s11f1+s12f1;syz =s22f1+s21f1;  fprintf('%2d \t\t%10.2e \t\t%10.2e\n',ii, sxz(ii), syz(ii));end%diary off

s11; %In-plane normal stresses in x-direction s12; %In-plane shear stresses in x-y plane;  s22 %In-plane normal stresses in y-direction;

 s21; %In-plane shear stresses in y-x plane; s13 % Out-of-plane shear stresses in x-z plane; s23; % Out-of-plane shear stresses in y-z plane;
disp('ENTER STRENGTH PARAMETERS');

 X=input('Tensile strength parameters'); XC=input('Compressive strength parameters'); Y=input('Lateral strength parameters');
YC=input('Compressive strength parameters'); SA=input('Shear strength parameters'); ST=input('Transverse strength parameters');

diary Fibre_failure_mode.out; Fibre-fracture =fopen('Fibre-fracture.txt', 'w');disp('PLY-BY-PLY FAILURE INDEX');

fprintf('===========Fibre-fracture Failures======\n'); fprintf(' ----------------------\n\n')

fprintf('Ply No     Normal & in-plane shear  \n'); %example for 24-Ply panel

for i= 1:24; fft(i)= (s11(i)./(X))^2+(1/(SA)^2)*(s12(i)^2+s23(i)^2);
```

```
    ffc(i) = s11(i)/XC; fprintf('%2d \t\t%10.2f \t\t\t\t%10.2f\n',i, fft(i),ffc(i));end; diary off
 diary matrix_failure_mode; Matrix-cracking =fopen('Matrix-cracking.txt', 'w')
fprintf('===========Matrix-cracking Failures======\n');fprintf('      ----------\n\n')
fprintf('=====      ================      ====================\n');
for i= 1:24; mft(i)= ((1./Y)^2)*(s22(i))^2+(1./(ST)^2)*(s13(i)^2)+...
    (1./(SA)^2)*(s12(i)^2+s23(i)^2);  %mfc(i)=(1./YC)*((YC/2*ST)^2-1)*(s22(i))+(1./4*ST^2)*(s22(i)^2)...
    %   +(1./ST^2)*(s13(i)^2)+(1./SA^2)*(s12(i)^2+s23(i)^2);  mfc(i)=(s22(i)./YC);
fprintf('%2d \t\t%10.2f \t\t\t\t%10.2f\n',i, mft(i),mfc(i));end; diary off
diary delamination_failure_mode; delamination =fopen('delamination.txt', 'w')
fprintf('===========De-lamination Failures======\n');fprintf('      ----------\n\n');
fprintf('=====      ================      ====================\n');
for i= 1:24; mft(i)= sqrt((1./SF13)^2)*(s13(i))^2+(1./(SF23)^2)*(s13(i)^2))%+...
    (1./(SA)^2)*(s12(i)^2+s23(i)^2);  %mfc(i)=(1./YC)*((YC/2*ST)^2-1)*(s22(i))+(1./4*ST^2)*(s22(i)^2)...
    %   +(1./ST^2)*(s13(i)^2)+(1./SA^2)*(s12(i)^2+s23(i)^2);  %mfc(i)=(s22(i)./YC);
fprintf('%2d \t\t%10.2f \t\t\t\t%10.2f\n',i, mft(i),mfc(i));end; diary off
```

4.2 Simulated results and discussions of 8-Ply panel impact with velocity 2m/s

Comparisons of in-plane normal and shear stresses obtained from Model 1 utilized fibre-fracture failure criteria predict no significant damage or ply level failure by flat impact. Similarly, comparisons of the stresses obtained from Model 2 predict no significant damage or ply level failure by flat impact. The comparisons are not reported, as failure or significant damage was not observed. Nonetheless, comparison of Model 2 obtained results by round nose predicts failure to ply 1 as depicted in column chart **FIGURE 16** and severe damage to ply 2.

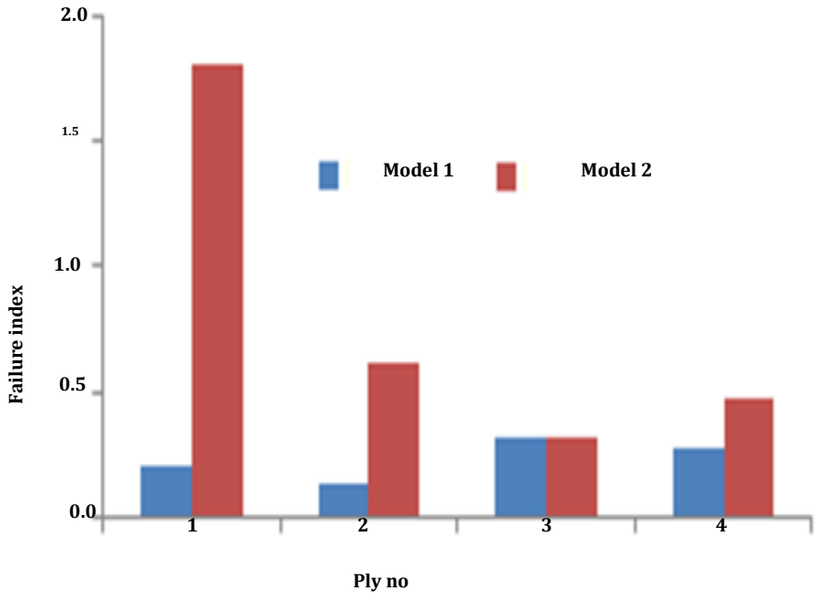

FIGURE 16: Fibre-fracture failure from simulated results by round nose impactor

Comparisons of in-plane normal and shear stresses obtained from Model 1 utilized in matrix-racking failure criteria predict no significant damage or ply level failure by flat impact. Similarly, comparisons of the stresses obtained from Model 2 predict no significant damage or ply level failure by flat impact. The comparisons are not reported, as failure or significant damage was not observed. Nonetheless, comparison of results by round nose predicts severe damage to ply 1 from Model 1 while failure to ply 1 and 2 as well as severe damage to ply 3 as depicted in column chart **Figure 17**.

ISSN: 2349 – 4891
Original Article

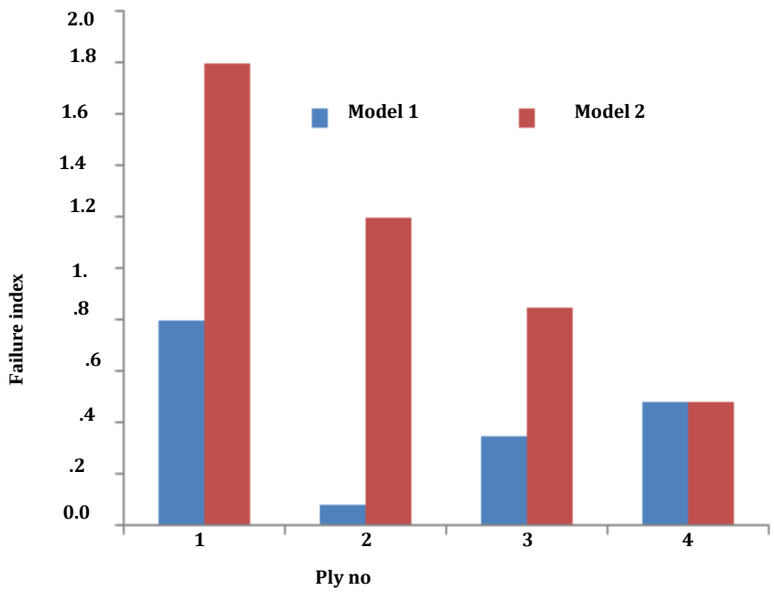

FIGURE 17: Comparison of matrix-cracking failure

Comparisons of transverse shear stresses obtained from impact of round nose impacts obtained from Model 1 utilized in quadratic delamination failure criteria predict no significant damage or ply level failure by flat and round nose impact. Similarly, comparisons of the stresses obtained from Model 2 predict no significant damage or ply level failure by flat impact. The comparisons are not reported, as failure or significant damage was not observed. Nonetheless, comparison of results by round nose predicts failure to ply 3 from Model 1 while failure to ply 3 and 4 as well as severe damage to ply 1 and 2 as depicted in column chart **Figure 18**.

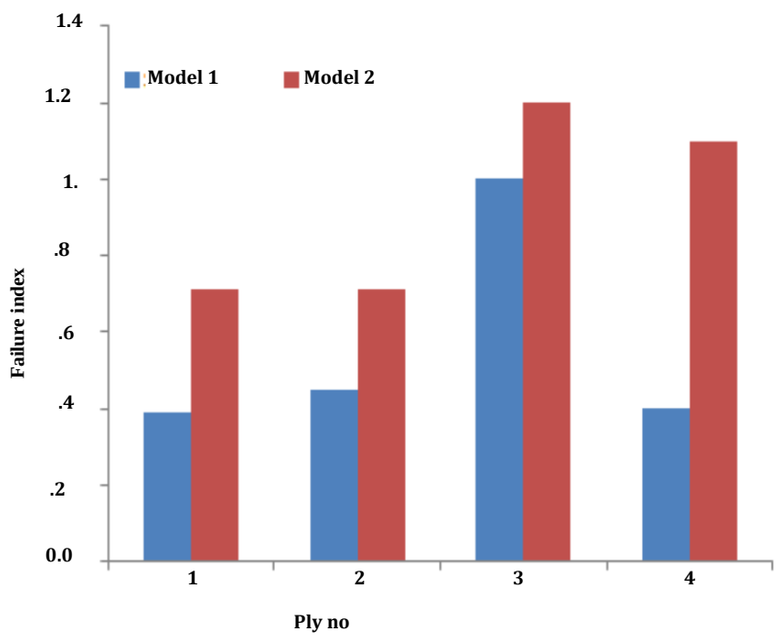

FIGURE 18: Quadratic delamination failure criteria

4.3 Failure predictions of 16-Ply panels with 3.12m/s impact velocity

Comparisons of in-plane normal and shear stresses obtained from un-partitioned and partitioned model with adaptive mesh models via matrix-cracking failure, matrix cracking criteria predicted no significant damage or ply level failure by flat impact and round nose impacts. Similarly, flat nose impacts from both the models show no significant damage or failure when in-plane as well as out-of-plane stresses were utilized in corresponding failure criteria. Thus, comparisons of results have not been included.

Comparisons of transverse shear stresses obtained from impact of round nose impacts obtained from Model 1 utilized in quadratic de-lamination failure criteria show significant damage to ply 1, 5 and 8 but no ply failure while Model 2

predicts failure to ply 1, 5, and 8 while severe damage to ply 6 as depicted in **FIGURE 19**.

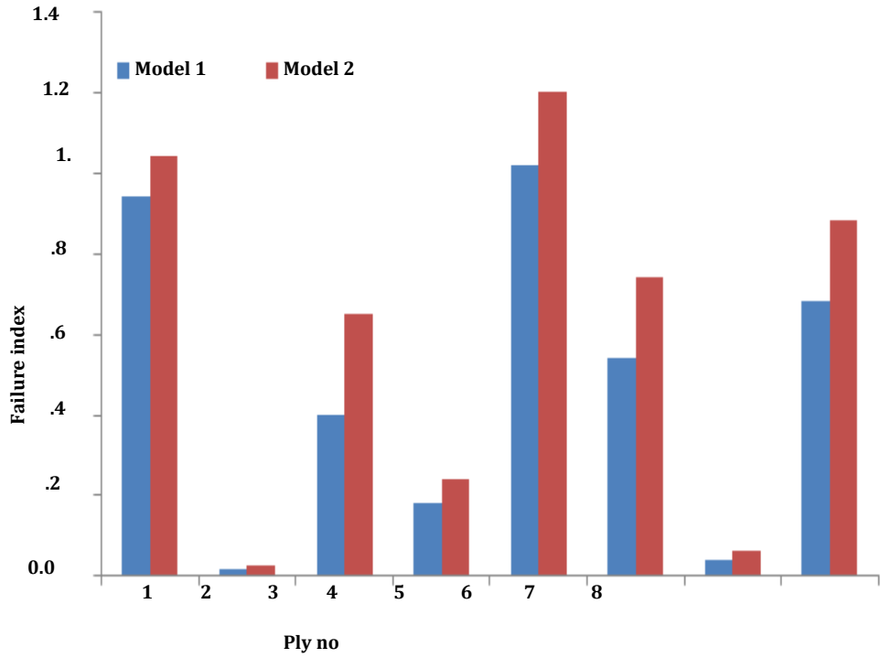

FIGURE 19: Ply by ply failure index of 16-Ply panels by round nose impacts

4.4 Failure predictions of 24-Ply panels impacted with 4.14m/s velocity

Comparisons of in-plane normal and shear stresses obtained from Model 1 and Model 2 utilized in fibre-fracture, matrix-fibre de-bonding failure criteria predicted no significant damage or ply level failure by flat impact and round nose impacts. Similarly, flat nose impacts from both the models show no significant damage or failure when in-plane as well as out-of-plane stresses were utilized in corresponding failure criteria. Thus, comparisons of results have not been included. Comparisons of transverse shear stresses obtained from impact of round nose impacts obtained from Model 1 utilized in quadratic de-lamination failure criteria predicts failure to ply 5 and significant damage to ply 1, 6 while Model 2 results predict failure to ply 1, 5, and 8 while severe damage to ply 6 as in **FIGURE 20**.

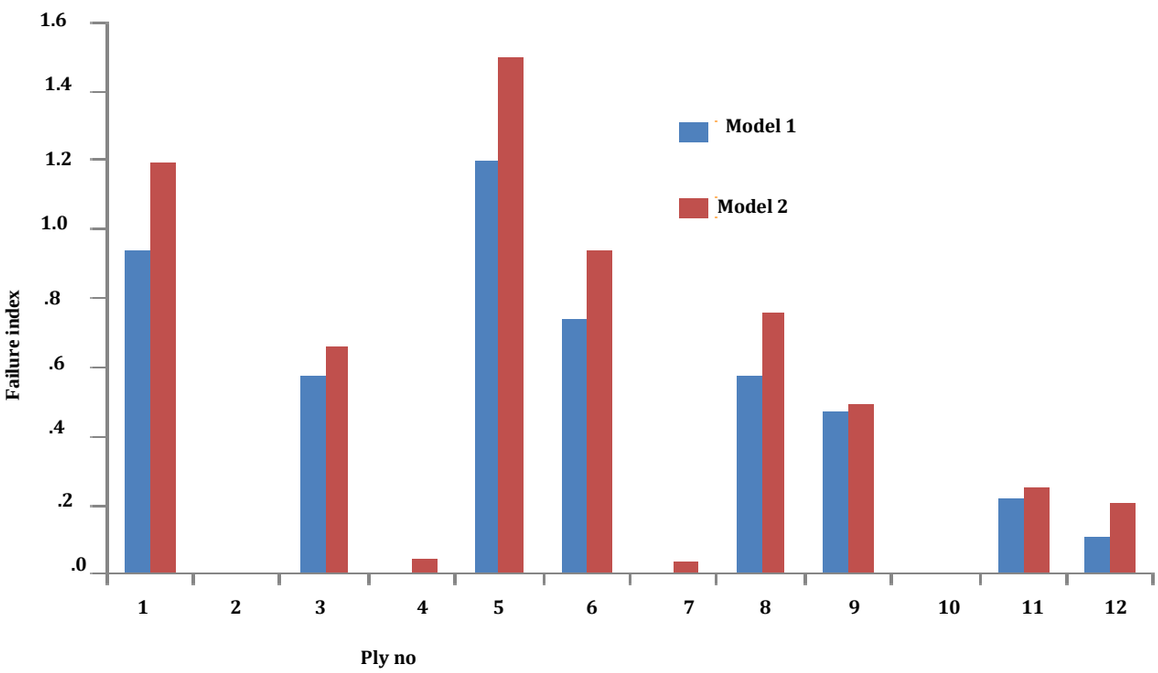

FIGURE 20: Ply by ply failure index of 24-ply panels by round nose impacts

Examination of stress based simulations and their comparison to experimental results demonstrate high level of consistency. The larger damaged area under the flat-nose curve indicates higher surface area damaged, high amount of energy absorption, relatively larger global damages, and inconsistencies with relatively impacts to thicker panels. Larger oscillations, load drops, and local damage were observed by round nose impacts. Experimental study provides knowledge about overall surface damage, however no potential damage or failure to a specific ply. The results obtained from Model 2 simulations confirmed in conjunction with fibre-

fracture, matrix-cracks, and quadratic-delamination failure criteria led to more ply level damage and failure.

5. Conclusions

In this work, computational models consisting of un-partitioned domain (Model 1) and partitioned domain with adaptive mesh (Model 2) were developed in ABAQUS™/Explicit software to simulate flat and round nose impacts of 8-, 16-, and 24-Ply panels. The non-destructive and data analyses of experimental tests provided base-line for computer simulations. The simulation Model 1 predicted failure of 16-Ply panel in delamination-mode of single ply, while simulation Model 2 predicted 2 plies failed. Furthermore, the simulation Model 2 predicted one ply fibre-failure, 2 matrix-cracking, and 2 delaminated failure plies in 8-Ply panel as well as 3 plies delaminated-mode failure in 24-Ply panel as shown in **Table 7**. Based on consistent comparisons, the following conclusions could be extracted from the results:

a) Experimental study provided base-line information, overall comparison for validation of computer simulations, and limitations of physical testing at ply level analysis.
b) Virtual partitioning of the high stress gradient region under impactor nose-tips generated dense elements with high refinement frequency adaptive meshing schemes.
c) More reliable three-dimensional stresses were efficiently computed from two-dimensional predicted stress by numerical integration through-the-thickness.
d) The predicted stress quantities were utilized in ply-by-ply fibre-fracture, matrix cracking, and de-lamination failure criteria that demonstrated more ply-level damage and failure.

TABLE 7: Ply-level failure predictions (Model 2)

Panel	Fibre-breakage Eq. (28)	Matrix-cracking Eq. (29)	Quadratic delamination Eq. (30)
8	1	2	3
16	0	0	2
24	0	0	3

Information could supplement the efforts underway in understanding complicated nature of impact event and determining reliable margins of safety with more confidence. The proposed study could be useful to simulate similar cases of different material property panels, lay-ups, stacking sequences, thicknesses, and impactors.

References

[1] Reddy J. N. Mechanics of Laminated Composite Plates and Shells Theory and Analysis 2nd ed. CRC Press Florida, USA 2004.

[2] Abrate S. Impact on composite structures. Cambridge University Press: Cambridge 2005.

[3] Robert M. Jones. Mechanics of Composite Materials 2nd ed. Taylor & Francis: Philadelphia, USA 1999.

[4] Standard Test method for Measuring the Damage Resistance of a Fibre-Reinforced Polymer-Matrix Composite to a Drop-Weight Impact Event, ASTM International 2005. D7136/D7136M-05, West Conshohocken, PA, 2005:1–16.

[5] James RA. Impact damage resistance and damage tolerance of fibre reinforced laminated composites (Ph.D. thesis), University of Bolton, United Kingdom, 2006.

[6] Panettieri E, Fanteria D, Montemurro M, Froustey C. Low-velocity impact tests on carbon/epoxy composite laminates: A benchmark study. Compos: Part B Eng 2016;107:9–21.

[7] Xiaozhou Gong, Pengying Pei, Yu Hu, Xiaogang Chen. Experimental investigation of low-velocity impact on textile cellular composite with different energy construction. J Ind Text 2019; 48(6):1009-1023.

[8] Standard Test method for Measuring the Damage Resistance of a Fibre-Reinforced Polymer-Matrix Composite to a Concentrated Quasi-static Indentation Force, ASTM International 2005. D6264-98(04), West Conshohocken, PA, 2005:1–16.

[9] Pierson MO and Vaziri R. Analytical solution for low velocity impact response of composite laminates. AIAA Journals 1996;34:1633-1640.

[10] Wishwas Mahesh, Jolandarshi Sharnappa, SM Kulkarni. Study on stacking sequence of plies in green sandwiches for low-velocity impact applications. Key Engg Mater 2019;801:59-64.

[11] Muhammad Ismail, Mohammad Jawaid. Low-velocity impact behaviour and post-impact characteristics of kenaf/glass hybrid composites with various weights. J Mater Res Technol, 2019;8(3):2662-2673.

[12] Shyr T-W, Pan Y-H. Impact resistance and damage characteristics of composite laminates. Compos Struct 2003;62:193–203.

[13] Davies GAO, Zhang X. Impact damage prediction in carbon composite structures. Int J Impact Eng 1995; 16:149-70.

[14] Hossein Taghipoor, Mohammad Darnghani Nouri. Experimental and numerical investigation of lattice core sandwich beam under low-velocity bending impact. J Sandwich Struct and Mater 2019;21(6):2154-2177.

[15] Sun CT and Liou WJ. Investigation of laminated composite plates under impact dynamic loading using a three-dimensional hybrid stress finite element method. Compos Struct 1989;(33):879-884.

[16] Ravandi M, Teo WS, Tran LQN, Yong MS, Tay TE. Low velocity impact performance of stitched flax/ epoxy composite laminates. Compos: Part B Eng 2017;117:89–100.

[17] Hashin, Z. Failure Criteria for Unidirectional Fibre Composites. J App Mech 47 1980;329–344.

[18] Jeifei Gu, Puhui Chen. Some modifications of Hashin's failure criteria for unidirectional composite materials. Compos Struct 2017;182:143-152.

[19] Schoeppner GA, Abrate S. Delamination threshold loads for low velocity impact on composite laminates. Compos: Part A Appl Sci Manuf 2000;31:903-15.

[20] Farooq U. Finite element simulation of flat nose low-velocity impact behaviour of carbon fibre composite laminates. PhD Thesis, University of Bolton, UK, 2014.

[21] Jiachen Zhu. Investigation of low velocity impact on advanced hybrid laminates Improving the impact resistance of CFRP laminates by embedding metal constituents. MSc Thesis, Delft University of Technology, Netherland, 2018.

[22] Sorough Sadeghnejad, Yousef Taraz Jamshidi, Reza Mirzaeifar, Mojtaba Sadighi. Modelling characteristics and parametric identification of low-velocity impact behaviour of time-dependent hyper-viscoelastic sandwich panels. J Mater Des Appl 2019;233(4):622-636.

[23] Ansari M, Chakrabarti A. Impact behavior of FRP composite plate under low to hyper velocity impact. Compos: Part B Eng 2016;95:462–74.

[24] Hongkarnjanakul N, Bouvet C, Rivallant S. Validation of low velocity impact modelling on different stacking sequences of CFRP laminates and influence of fibre failure. Compos Struct 2013;106:549–59.

[25] Borg R, Nilsso L, Simonsson K. Simulation of low velocity impact on laminates using a cohesive zone based delamination model. Compos Sci Technol 2004;64:279-88.

[26] Riccio A, Luca A De, Felice G Di, Caputo F. Modelling the simulation of impact induced damage onset and evolution in composites. Compos: Part B Eng 2014;66:340–7.

[27] Shi Y, Swait T, Soutis C. Modelling damage evolution in composite laminates subjected to low-velocity impact. Compos Struct 2012;94:2902–13.

[28] Shi Y, Pinna C, Soutis C. Modelling impact damage in composite laminates: A simulation of intra- and inter-laminar cracking. Compos Struct 2014;114:10–9.

[29] Falzon BG, Apruzzese P. Numerical analysis of intra-laminar failure mechanisms in composite structures. Part I: FE implementation. Compos Struct 2011;93:1039–46.

[30] Falzon BG, Apruzzese P. Numerical analysis of intra-laminar failure mechanisms in composite structures. Part II: Applications. Compos Struct 2011;93:1047–53.

[31] Feng D, Aymerich F. Finite element modelling of damage induced by low-velocity impact on composite laminates. Compos Struct 2014;108:161-71

[32] Payen DJ, Bathe KJ. A stress improvement procedure. Comput Struct 2012;112- 113:311– 26.

[33] Farooq U, Myler P. Efficient computational modelling of carbon fibre reinforced laminated composite panels subjected to low-velocity drop-weight impact. Mater Des 2014;54:43–56.

[34] Farooq U, Myler P. Finite element simulation of damage and failure predictions of relatively thick carbon fibre-reinforced laminated composite panels subjected to flat and round noses low-velocity impact Thin-Walled Struct 2016;104:82-105.

[35] Kim J, Bathe KJ. The finite element method enriched by interpolation covers. Comput Struct 2013;116:35–49.

[36] Takashi Misaka, Daisuke Sasaki, Shiegeru Obayashi. Adaptive mesh refinement and local balancing based on multi-level block-structured Cartesian mesh. Int J Comp Flu Dyn 2017;31(10):476-487.

[37] Oguibe CN and Webb DC. Finite element modelling of the impact response of laminated composite plates. Compos Sci Technol 1999;(59):1913-1922.

[38] Bathe KJ, Noh G. Insight into an implicit time integration scheme for structural
dynamics. Comput Struct 2012;98–99:1–6.

[39] Nsiampa N, Ponthot J, Noels L. Comparative study of numerical explicit schemes for impact problems. Int J Imp Eng 2008;35:1688–94.

[40] Shi Y, Pinna C, Soutis C. Modelling impact damage in composite laminates: A simulation of intra- and inter-laminar cracking. Compos Struct 2014;114:10–9.

[41] Mahajan P. Contact behaviour of an orthotropic laminated beam indented by a rigid cylinder. Compos Sc Technol 1998;58:505-13.

[42] Falzon BG, Apruzzese P. Numerical analysis of intralaminar failure mechanisms in composite structures. Part I: FE implementation. Compos Struct, 2011;93:1039–46.

[43] Falzon BG, Apruzzese P. Numerical analysis of intralaminar failure mechanisms in composite structures. Part II: Applications. Compos Struct, 2011;93:1047–53.

[44] Chung J, Lee JM. A new family of explicit time integration methods for linear and nonlinear structural dynamics. Int J Num Meth Eng 1994;37:3961–76.